MULTI-STRUCTURE TURBULENCE IN A BOUNDARY LAYER WITH A UNIFORMLY SHEARED FREE STREAM

by
Curtis Livingston

A thesis submitted to
the Faculty of Mechanical Engineering
in partial fulfillment of
the requirements for the degree of

MASTER OF APPLIED SCIENCE

in Mechanical Engineering

Ottawa-Carleton Institute for Mechanical and Aerospace Engineering
University of Ottawa
Ottawa, Canada

Abstract

A turbulent boundary layer (TBL), generated in a water tunnel, extended to a highly turbulent and anisotropic "free stream" that consisted of a uniformly sheared flow (USF) with a mean shear that was in the opposite direction to that in the TBL. Extensive measurements of the fluctuating velocity were taken with the use of hot-film anemometry, laser Doppler velocimetry and particle image velocimetry. On either side of the TBL edge, defined as the location of maximum velocity, the turbulence relaxed to its canonical structures in TBL and USF, respectively, but, in the vicinity of the edge, the turbulence was multi-structure and exhibited strong departures from canonical behaviour. Of particular interest was the variation of the dissipation parameter, which, in contrast to its near-constancy in well-developed canonical flows, varied inversely proportionally to the turbulence Reynolds number. The entire flow contained horseshoe-shaped coherent structures, whose properties, however, varied from the TBL, across the multi-structure region and into the USF.

Acknowledgements

I would like to first and foremost thank Dr. Stavros Tavoularis for the opportunity to perform research under his supervision. I am grateful for the knowledge and expertise he shared with me during the completion of this thesis.

I recognise the financial support of the Natural Sciences and Engineering Research Council of Canada which funded the thesis and associated costs enabling my entire focus to be towards my research.

The machine shop personnel were always very helpful in determining if designed components were feasible to manufacture and would gladly provide an opinion on equipment maintenance if requested.

Dana Duong, Azim Bin Mohd Arshad, Abderrazzak Mouslim, and Marc-Étienne Lamarche-Gagnon were always willing to answer my numerous questions and I hope they managed to put up with my occasional sarcasm. Their advice and ears were instrumental in helping me solve problems during my work within the laboratory and I enjoyed attempting to do the same in return.

I would like to thank Christina Vanderwel for providing her superb MATLAB programs which enabled simpler analysis of the vector fields from the PIV measurements and for leaving excellent instructions on how to setup and use the water tunnel and related equipment.

I am very grateful for my great-aunt and -uncle, emphasis on the 'great', for providing me food, water, and shelter as I worked on my thesis.

Lastly, I need to thank my partner, Jacqueline Parco, for her unwavering support and consistent pressure to do my best work on the thesis and in life.

Table of Contents

List of Tables

List of Figures

Nomenclature

C_s'	representation of the number of large scale eddies within a flow
C_ϵ	dissipation parameter
G	constant which relates voltage and velocity in hot-film measurements
h	height between upper and lower walls in the test section
k	turbulent kinetic energy
l	length of test section
L	integral length scale
$\mathcal{L}$	internal length scale
Re_δ	Reynolds number based on the size of the boundary layer
Re_x	Reynolds number based on the distance travelled streamwise
Re_λ	turbulence Reynolds number based on the Taylor microscale
Re_θ	Reynolds number based on the momentum thickness in the turbulent boundary layer
U_i	fluctuating velocity
$U_{1\mathrm{max}}$	maximum streamwise velocity
U_∞	free stream velocity
u_i	velocity fluctuation
w	width of test section
x_i	position vector in the test section

Greek symbols

δ boundary layer thickness

ϵ rate of dissipation of turbulent kinetic energy

θ momentum thickness

η Kolmogorov microscale

λ Taylor microscale

ν kinematic viscosity of the fluid

ρ shear stress correlation coefficient

ρ_f density of fluid

Other notation

$\overline{(...)}$ time average

$(...)'$ standard deviation

Acronyms

CCW counter-clockwise

CW clockwise

DAS data acquisition system

DNS direct numerical simulation

HFA hot-film anemometry

LDV laser Doppler velocimetry

PDF probability density function

PIV particle image velocimetry

PVC polyvinyl chloride

RMS root mean square

SD standard deviation

SSCC shear stress correlation coefficient

TBL turbulent boundary layer

TKE turbulent kinetic energy

USF uniformly sheared flow

Chapter 1

Introduction

1.1 Motivation

Turbulent flows have been the focus of many studies over the years. The flows which have been researched the most are canonical flows, which are geometrically simple and easily reproducible in the laboratory. These include, among others, two dimensional boundary layers, axisymmetric jets and pipe flows. Canonical flows themselves are a very small subset of turbulent flows, but they retain some features which are also encountered in broad ranges of turbulent flows. The vast majority of turbulent flows in natural and industrial systems are non-canonical. Because of the diversity and possible complexity of strongly non-canonical flows, information collected for one such flow is rather unlikely to apply to many others. For this reason, a meaningful strategy for expanding our understanding of turbulence seems to be to examine flows with specially designed, mildly non-canonical features. One such example would be a canonical flow that is distorted by an external device or mechanism, which may eventually fade away or be removed. Another example would be the interaction region between two canonical flows. Such flows, either in their entirety or in limited regions, would have non-canonical structures which are the results of more than one distinct turbulence generation mechanisms; they have recently been termed *multi-structure turbulence* (Nedić and Tavoularis, 2018).

Turbulent boundary layers (TBL) are the most intensely researched turbulent flow. In the majority of studies, the TBL was subjected to a nominally uniform, laminar free stream, in which case the TBL would have a canonical structure. In a few cases, TBL have been exposed to a free stream with some weak, decaying turbulence, usually generated by an upstream grid. The latter TBL would have a multi-structure region, but the deviation from the canonical structure would disappear as free-stream turbulence decays. Another type of a canonical turbulent flow is the uniformly sheared

flow (USF). In USF, turbulence not only does not decay downstream, but actually becomes intensified, as the result of an active turbulence production mechanism. Although turbulence is generated by the mean shear in both TBL and USF and there are structural similarities between outer TBL and USF, there are also some significant differences: a) in TBL, mean shear is produced by friction with the wall, whereas, in USF, mean shear is imposed in the absence of a wall; b) in TBL, the wall also imposes a kinematic constraint, which is absent in USF; c) TBL are separated from the free stream by a thin interface, whereas USF are ideally unbounded in all directions; and d) the turbulence in TBL is inhomogeneous, whereas, in USF, turbulence is homogeneous, at least on planes normal to the flow direction. In view of these considerations, the interaction region between a TBL and a uniformly sheared, highly turbulent free stream evolving in parallel seems to be a promising environment for the study of multi-structure turbulence, which is the product of two distinct, persisting and canonical turbulence generation mechanisms. Most of the turbulence activity, namely the motions that contain most of the turbulence kinetic energy, is associated with *coherent structures*, defined as identifiable, organised, recurring, large-scale flow patterns, which are distinct from background, random, not organised turbulent motions (*non-coherent turbulence*). In both TBL and USF, the dominant coherent structures, at least at moderate Reynolds numbers, are horseshoe- or hairpin-shaped vortices. In TBL, these structures form in packets with a leading vortex and multiple vortices trailing behind (Adrian, 2007). Packets of horseshoe vortices have also been detected in USF (Vanderwel and Tavoularis, 2011). An important point of interest would be to examine how the coherent structures that are generated in a TBL interact with those generated in a USF in the multi-structure region between the two flows. Turbulence theories and models require the use of a length scale and a time scale, or equivalently a velocity scale and a length scale, which characterise the dominant motions and by which one can scale the various statistical properties that appear in the governing equations. An obvious choice for a velocity scale is one that is proportional to the square root of the turbulent kinetic energy per unit mass k. There is also an obvious internal length scale, one that corresponds to the size of the energy

containing motions: the integral length scale L. The definition of this scale, however, requires consideration of spatial variations of turbulent motions, information which is not contained in the single-point differential equations that describe local turbulence. Therefore, there is a need to define a surrogate length scale in terms of local variables, namely variables that are contained in the single-point turbulence equations. Besides k and other variables, these equations contain the turbulent kinetic energy dissipation rate per unit mass ϵ. Although mechanical kinetic energy is dissipated to heat by very small size "eddies", the total ϵ is set by the energy containing motions. These motions set the rate by which kinetic energy that is produced at large scales is fed successively to smaller eddies, following the *energy cascade process*, until it reaches the smallest eddies, where it is dissipated. Then, it is easy to define a surrogate length scale $\mathcal{L}$ by dimensional analysis, namely, by multiplying appropriate powers of k and ϵ. This provides the result $\mathcal{L} \propto k^{3/2}/\epsilon$.

A cornerstone assumption of turbulence theories and models is that $\mathcal{L} \propto L$ or, equivalently, that the *dissipation parameter* $C_\epsilon \propto L/\mathcal{L}$ is constant. This assumption has been shown to hold approximately for extensive regions of many canonical flows, in which various turbulence properties evolve in a commensurate manner. Nevertheless, there is also a growing body of evidence contradicting this hypothesis in both upstream regions of canonical turbulence and in multi-structure turbulence (Nedić and Tavoularis, 2018; Nedić et al., 2017; Vassilicos, 2015). Testing this hypothesis in the multi-structure region between a TBL and a USF and understanding the relationship among these scales and other flow properties would be of value in explaining the limitations and failures of current turbulence models and developing improved ones.

1.2 Objectives

The general goal of this research is to enlarge the available documentation on multi-structure turbulence, particularly one that pertains to TBL. The specific goal is to document experimentally the turbulence in a TBL that is bounded by a highly turbulent, uniformly sheared free stream that has a mean shear opposite in direction to the one inside the TBL. Extensive measurements will be obtained using hot-film anemometry, laser Doppler velocimetry and particle image velocimetry. Measurements will

include transverse profiles of the mean velocity, the Reynolds stresses, the integral length scales, the Taylor and Kolmogorov microscales. The measurements will be used to calculate the mean velocity gradient, the turbulence anisotropies, the shear stress correlation coefficient, the turbulent kinetic energy and its dissipation rate, the turbulence Reynolds number Re_λ and the dissipation parameter. The results will characterise the behaviour of the dissipation parameter within the interaction region and its possible relationship to Re_λ or other flow properties. The statistical properties of coherent structures in USF, the TBL and the multi-structure region will also be determined and compared.

1.3 Organisation of the thesis

This thesis consists of six chapters with this introduction being the first. The second chapter outlines some background information on USF and TBL and provides insight into the relevant literature on these flow types. Chapter 3 describes the experimental facilities and instrumentation. The fourth chapter outlines the procedures used with each of the measurement techniques. Chapter 5 describes the collected measurements, discusses the results and compares them to results from other studies. Finally, Chapter 6 contains the main conclusions of this work and recommendations for future research.

Chapter 2

Analytical Background and Literature Review

This chapter describes briefly the definitions of the basic properties of turbulent flows and summarises the essential literature on turbulent boundary layers, uniformly sheared flows, multi-structure turbulence and the dissipation parameter.

2.1 Definitions of Basic Properties of Turbulence

A common approach for the analytical description of turbulent flows is to employ the Reynolds decomposition, by which a random variable is decomposed into a mean and a fluctuation. For stationary turbulent flows, namely flows that have statistical properties that are independent of a shift in time origin, Reynolds decomposition for the instantaneous flow velocity U_i in Cartesian coordinates $x_i, i = 1, 2, 3$, is written as

$$U_i = \overline{U}_i + u_i \ , \tag{2.1}$$

where $\overline{U}_i$ is the time average and u_i is the velocity fluctuation. In the following, overbars will denote time averages and lower case symbols will denote mean-free fluctuations. The Reynolds stress tensor, or turbulent stress tensor, is defined as $-\rho_f \overline{u_i u_j}$, where ρ_f is the fluid density. The same name is frequently used for the simpler tensor $\overline{u_i u_j}$. This tensor consists of three normal stresses $\overline{u_1^2}, \overline{u_2^2}, \overline{u_3^2}$ and three independent shear stresses $\overline{u_1 u_2}, \overline{u_1 u_3}, \overline{u_2 u_3}$. For flows with a mean velocity that is nearly parallel to the x_1 axis and a mean velocity gradient that is nearly parallel to the x_2 axis, an important parameter is the shear stress correlation coefficient

$$\rho = -\frac{\overline{u_1 u_2}}{u_1' u_2'} \ . \tag{2.2}$$

The standard deviation (SD) of the fluctuations of each velocity component will be denoted by a prime as, for example,

$$u_i' = \sqrt{\overline{u_i^2}} \ . \tag{2.3}$$

The turbulent kinetic energy (TKE) per unit mass is defined as

$$k = \frac{1}{2}\left(\overline{u_1^2} + \overline{u_2^2} + \overline{u_3^2}\right) \tag{2.4}$$

and the rate of turbulent kinetic energy dissipation to heat per unit mass is defined as

$$\epsilon = \frac{1}{2}\nu\overline{\left(\frac{\partial u_i}{\partial x_j} + \frac{\partial u_j}{\partial x_i}\right)\left(\frac{\partial u_i}{\partial x_j} + \frac{\partial u_j}{\partial x_i}\right)} \ . \tag{2.5}$$

Three different length scales are commonly used to characterise the size of motions that dominate different activities. The integral length scale characterises the size of the energy containing eddies. Although integral length scales can be defined in different directions, most commonly used is the streamwise integral length scale, defined as

$$L = \int_0^{r_{10}} \frac{\overline{u_1(x_1 + r_1)u_1}(x_1)}{\overline{u_1^2}} \ dr_1 \ , \tag{2.6}$$

where r_{10} is the first zero of the integrand, which is the streamwise auto-correlation coefficient. The size of motions that contribute mostly to the energy dissipation is characterised by the Kolmogorov microscale

$$\eta = \left(\frac{\nu^3}{\epsilon}\right)^{1/4} \ . \tag{2.7}$$

Finally, a scale intermediate between L and η is the Taylor microscale, defined as

$$\lambda = \frac{{u_1}'}{\sqrt{\overline{(\frac{\partial u_1}{\partial x_1})^2}}}. \tag{2.8}$$

Under the assumption of local isotropy, one may estimate ϵ as

$$\epsilon \approx \frac{15\nu {u_1}'^2}{\lambda^2} \tag{2.9}$$

The relative strength of turbulent activity is characterised by the turbulence Reynolds number

$$\mathrm{Re}_\lambda = \frac{u_1'\lambda}{\nu} \ . \tag{2.10}$$

2.2 Turbulent Boundary Layers

2.2.1 Definitions

A boundary layer is a relatively thin region of fluid that forms for sufficiently large Reynolds numbers and where the flow is affected significantly by friction with a solid wall. Depending on the conditions, boundary layers can be entirely laminar or entirely turbulent, or they may contain a region in which transition to turbulence occurs. The turbulence within a TBL is inhomogeneous and anisotropic. Compared to laminar boundary layers at the same Reynolds number, turbulent boundary layers have greater rates of heat transfer and mixing as well as a higher wall shear stress. A common convention in fluid mechanics is the no-slip condition, which means that fluid in contact with a solid wall will move at the same velocity as the wall. This condition implies that, for a stationary surface, the fluid directly in contact will also be stationary. As distance from the wall increases, the velocity of the fluid increases until it essentially matches (within 99%) the free stream velocity U_∞, which happens at a distance δ, referred to as the physical boundary layer thickness. This thickness is defined rather arbitrarily and is difficult to determine accurately. Instead, a more commonly used scale is the momentum thickness, defined as

$$\theta = \int_0^\infty \frac{\overline{U}_1(x_2)}{U_\infty}\left[1 - \frac{\overline{U}_1(x_2)}{U_\infty}\right] dx_2 \approx \int_0^\delta \frac{\overline{U}_1(x_2)}{U_\infty}\left[1 - \frac{\overline{U}_1(x_2)}{U_\infty}\right] dx_2 \ . \tag{2.11}$$

The development of a boundary layer is characterised by three different Reynolds numbers, corresponding to the streamwise distance x_1 from the origin, the physical thickness δ and the momentum thickness θ. These are, respectively, defined as follows:

$$\mathrm{Re}_x = \frac{U_\infty x_1}{\nu}, \tag{2.12}$$

$$\mathrm{Re}_\theta = \frac{U_\infty \theta}{\nu} \tag{2.13}$$

and

$$\mathrm{Re}_\delta = \frac{U_\infty \delta}{\nu}. \tag{2.14}$$

2.2.2 Coherent Structures in Turbulent Boundary Layers

It has been well established that the dominant coherent structures in TBL are horseshoe/hairpin vortices (Figure 2.1), generally consisting of two legs and a head. These structures were first identified by Theodorsen (1952) and have been the subject of many experimental and computational studies. Head and Bandyopadhyay (1981)

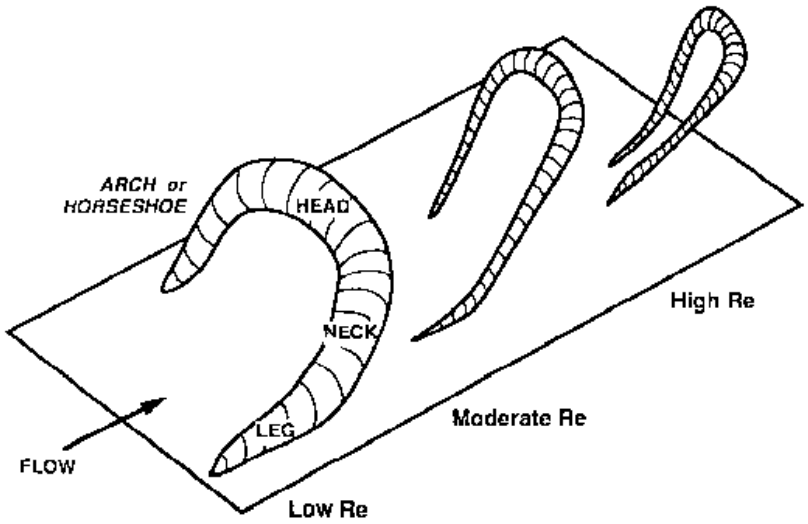

Figure 2.1: The general shape of horseshoe and hairpin vortices; reproduced with permission from Robinson (1991).

provided a description of these coherent structures based on flow visualisation using smoke. For relatively small Reynolds numbers, portions of roller vortices that appear near the wall get lifted away from the wall to form a horseshoe-shaped structure. The head of this horseshoe travels faster than the legs, which trail behind, so that the structure is inclined by an angle between 40° and 50°. For larger Reynolds numbers, these structures are more stretched and resemble hairpins and, when Re_θ exceeds a certain threshold, the structures lack a well-defined shape. In the boundary layer, these structures contain a self-sustaining instability mechanism, as the conditions on the surface of the wall after a coherent structure has passed are ideal for another coherent structure to form.

Robinson (1991) reviewed previous literature on coherent structures in the TBL and stated that horseshoe vortices have heights that are comparable to their widths, whereas hairpin vortices have elongated legs and are often lopsided. According to

Adrian et al. (2000), the large scale motions in the TBL are made up of groups of hairpins, referred to as packets. Hairpins that last longer in the flow are considered to be mature and make up the bulges in the interface between the TBL and the free stream. Adrian (2007) further researched the organisation of these packets in the TBL using direct numerical simulations (DNS). He confirmed the observation of Head and Bandyopadhyay (1981) that the formation of a hairpin also created ideal conditions for other structures to form both upstream and downstream. Such conditions only occur when the initial hairpin has a large enough magnitude but creates a birthing process known as auto-generation. Adrian also discerned that, if there was any spanwise velocity during the formation of the vortex, it would no longer be symmetrical and would resemble a hook or cane, in agreement with results by Robinson (1991). Among the several DNS investigations of zero-pressure-gradient boundary layers, worth mentioning is the one by Wu and Moin (2009), which analysed the transition to turbulence as well as the evolution of structural components throughout this process. These authors found proof that the destruction of a hairpin vortex can cause a packet of other vortices to form from the two legs of this vortex.

2.3 Uniformly Sheared Flow

2.3.1 Flow Description

An idealised turbulent flow is the homogeneous shear flow (HSF), which has a linear velocity profile, homogeneous turbulence and is unbounded. Such flow cannot be generated in the laboratory, but it has been approximated by uniformly sheared flow, which has been generated in wind- and water-tunnels by passing a stream through a device with transversely varying blockage (shear generator). To ensure that the integral length scale is transversely uniform, at least initially, a second device (flow separator) that separates the stream into parallel channels with equal heights is commonly used. Sufficiently downstream of this device, the mean velocity has a uniform gradient and can be represented as

$$\overline{U}_1 = \frac{d\overline{U}_1}{dx_2} x_2,\ \overline{U}_2 = 0,\ \overline{U}_3 = 0\ . \tag{2.15}$$

The turbulence in USF is approximately homogeneous on transverse planes, although it grows in the streamwise direction due to its production by the mean shear that counteracts the dissipation. The turbulence in USF is strongly anisotropic and its anisotropy level is comparable to the one in the outer region of TBL.

2.3.2 Coherent Structures in Uniformly Sheared Flow

The coherent structures that dominate the turbulence in USF are, like in TBL, horseshoe-shaped vortices. In TBL, vortices have previously been detected only forming with their heads oriented away from the wall, namely toward the higher-velocity region. In USF, however, vortices were found with their heads pointing toward both higher- and lower-velocity regions. Rogers and Moin (1987) examined the structure of homogeneous shear flow using DNS. They found that the dominant coherent structures were hairpin vortices that were formed when vorticity created spanwise roller-type vortices, parts of which lifted away to form heads of horseshoe vortices. The angle of these structures was initially 45° with respect to the flow direction and, as the flow developed, it was reduced to between 35° and 40°. A DNS analysis of homogeneous shear flow was also performed by Kida and Tanaka (1992), who identified hairpin-shaped structures that were generated by the roll up of vortex sheets into tubes and observed strong Reynolds shear stress between the two legs of the hairpins.

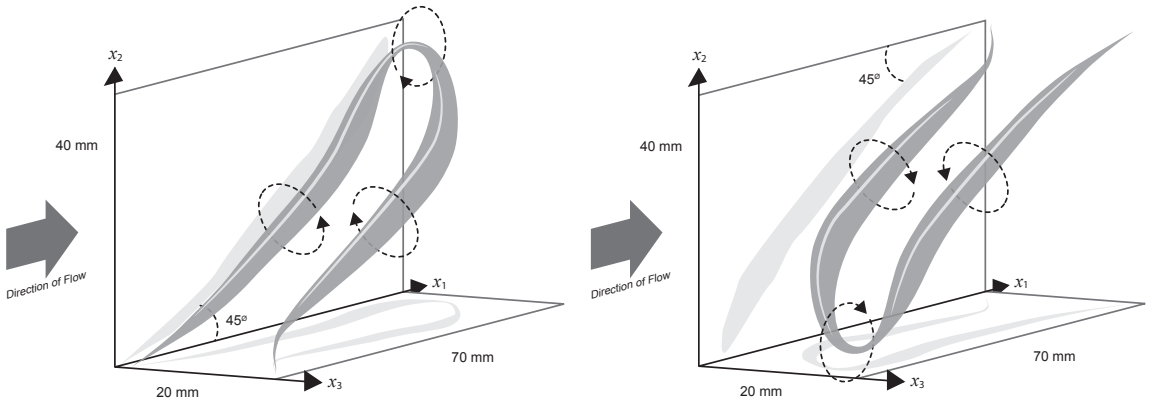

(a) Upright horseshoe vortex. (b) Inverted horseshoe vortex.

Figure 2.2: Artistic view of upright and inverted horseshoe vortices; the local vortex diameter in the sketches does not correspond accurately to the local vortex core size; reproduced with permission from Vanderwel and Tavoularis (2011).

Kislich-Lemyre (2003) used flow visualisation in a USF generated in the same water tunnel as the one used in this study. He describes the dominant coherent structures as resembling hairpin-type vortices, in agreement with past DNS studies (Kida and Tanaka, 1992; Rogers and Moin, 1987). Kislich-Lemyre (2003) noticed that, as the structures developed in the flow, they became distorted and stretched, suggesting the cause of this being either a Magnus effect or the lifting effect from in between the two vortex legs, which are a pair of counter-rotating vortices. A thorough investigation of the structure of USF in the same water tunnel was conducted by Vanderwel and Tavoularis (2011). These authors identified structures that resembled horseshoe-shaped vortices with orientations of their heads pointing both towards higher- and lower-velocity regions, which they termed as upright and inverted horseshoe vortices (Figure 2.2). More recently, Dong et al. (2017) performed a DNS study of HSF and observed vortex clusters. They also detected hairpins, that were more hook-shaped than in some of the TBL studies previously mentioned. These hooks formed as part of diagonal rollers that became more streamwise near the walls.

2.4 Multi-structure Turbulence

The term multi-structure turbulence signifies flows or regions of flows in which turbulence is generated by two or more distinct production mechanisms. The local structure can not be described as canonical, but it may have features of one or multiple canonical flows. In some cases, multi-structure turbulence may relax to a canonical state with a single production mechanism.

Although the term multi-structure turbulence was first used in 2018 (Nedić and Tavoularis, 2018), many previously studied turbulent flows have multi-structure regions. One example is the study by Charnay et al. (1971), which examined the development of a TBL with different free stream turbulence levels. These authors found that, as the free stream turbulence was intensified, the boundary layer grew faster. Additionally the wall and turbulent shear stresses were larger and the production of turbulent kinetic energy was increased. Studies of multi-structure turbulence in TBL with turbulent free streams were also conducted by Evans (1974), Meier and Kreplin (1980) and Hoffmann et al. (1989). In all these studies, the free stream turbulence

was grid-generated and essentially isotropic. In contrast, Liangwei and Hoffmann (1988) investigated TBL in free streams with anisotropic turbulence, which was generated by bars of different diameters and in which the streamwise turbulent stresses were smaller than in isotropic turbulence, but the normal and spanwise stresses were significantly larger. These authors determined that both anisotropic and isotropic free stream turbulence had comparable effects on the boundary layer thickness and the skin friction.

Kislich-Lemyre (2003) investigated how the large-scale structure of USF was distorted by a solid wall, which was stationary or moving in the same or opposite direction to the flow. When the wall moved faster than the flow, a region of low or zero shear was detected between the wall boundary layer and the free stream USF. Distinct coherent structures were observed on the two sides of this region, which is a region of multi-structure turbulence. Unfortunately, the documentation of this study has been mostly qualitative. A different study of multi-structure turbulence is the one performed by Sakai et al. (2013), which describes the effect of the wake of a cylinder in the free stream on the turbulent statistics of a TBL. This study found that the inner layer mean flow velocity profile was not altered by the presence of a cylinder wake, but the intensity of the turbulence decreased.

Nedić and Tavoularis (2018), who introduced the term multi-structure turbulence, examined the distortion of a fully developed USF by grid-generated turbulence. Far from the inserted grid, its turbulence decayed and the flow structure relaxed to the USF structure, but some permanent offsets remained on the values of the length scales, the turbulent stresses and the turbulence Reynolds number.

2.5 Dissipation Parameter

Different authors have defined the dissipation parameter using different expressions for the length scale and the velocity scale. In this study, we will use the following definition

$$C_\epsilon = \frac{\epsilon L}{{u_1}'^3} \ . \tag{2.16}$$

This definition is based on values of properties in the streamwise direction, which are measurable with the available instrumentation. Pearson et al. (2002) examined

the change of the dissipation parameter as Re_λ was increased and concluded that, as $\mathrm{Re}_\lambda \to \infty$, the dissipation parameter approached a constant value, which depended on the way the different scales were calculated and the flow conditions. Burattini et al. (2005) also concluded that there was no obvious universal limit of the values of the dissipation parameter. According to these authors, the dissipation parameter values would be the same only in identical flows with the same initial conditions. Mazellier and Vassilicos (2008) explored the constancy of the dissipation parameter with respect to the large-scale flow structure and found that the C_ϵ value scaled with another dimensionless term, C_s', which represents the number of large-scale eddies in a flow and takes different values in different flows. By accounting for C_s', the values of C_ϵ tended to a specific constant value for each different flow type. This was referred to as the eventual Re_λ independence of C_ϵ.

A review of previous theoretical and experimental research concerning the dissipation parameter was presented by Vassilicos (2015). One of the groups of flows considered, includes forced statistically stationary turbulence created using DNS in a periodic or a closed box. Vassilicos noted that in such cases the dissipation parameter tended to a constant value, which, however, depended on the inlet conditions. Another group was decaying turbulence. A compilation of the available C_ϵ values demonstrated that there was a region in which, as the turbulence decayed, the C_ϵ value increased, but once a certain streamwise location in the flow was reached, C_ϵ instantaneously became constant. The evolution of the dissipation parameter in developing USF was examined by Nedić and Tavoularis (2016). Following a full development of the turbulence structure, the dissipation parameter maintained a constant value of 0.56, which was possibly specific to the inlet conditions in this flow.

Djenidi et al. (2017) examined the dissipation parameter in grid and jet turbulence and found that in both cases C_ϵ became constant downstream of a certain location. Nedić et al. (2017) discussed the scaling of C_ϵ in constant pressure turbulent boundary layers. While the value of the dissipation parameter varied with distance from the wall, C_ϵ tended to be constant in the streamwise direction for sufficiently large values of the momentum thickness Reynolds number. Nedić and Tavoularis (2018) examined C_ϵ in a USF distorted by a grid. C_ϵ depended on the local Re_λ in the multi-structure

region and relaxed to a constant after grid turbulence decayed, but the value of this constant was different from the one in undistorted, fully developed USF. This agrees with previous results that the inlet conditions have a very significant effect on the dissipation parameter in the flow.

Chapter 3

Experimental Facilities and Instrumentation

This chapter describes the facilities and different pieces of equipment and instrumentation used for the experiments. These include the water tunnel, the shear generator and flow separator, the upper wall, the traversing systems, laser Doppler velocimetry, particle image velocimetry, the particles added to the flow, and hot-film anemometry.

3.1 Water tunnel

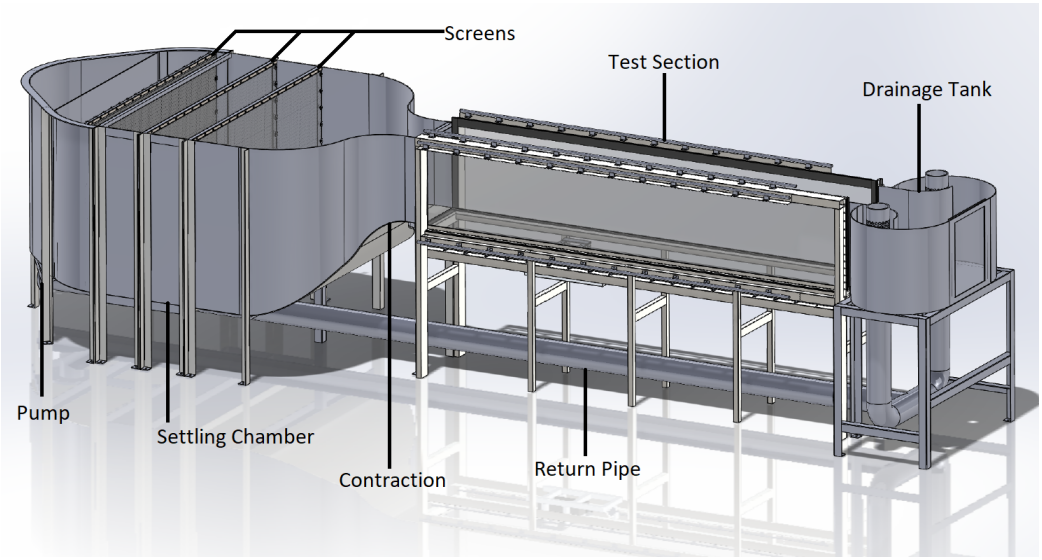

Figure 3.1: The water tunnel at the University of Ottawa.

The experiments were performed in the recirculating water tunnel at the University of Ottawa, which can hold up to approximately 15,000 liters of water (Figure 3.1). The water tunnel has six main sections: the settling chamber, the contraction, the test section, the drainage tank, the return pipe and the pump. The majority of the water is stored in the settling chamber, which contains several perforated plates, a porous sheet and an 8.6:1 contraction, which make the stream entering the test section more

uniform and decrease its fluctuation level.

The test section is a rectangular prism open at the top and with its sides and bottom made out of three full-length pieces of glass. The length of the test section is 4.1 m, its height is 0.74 m, and its width is 0.56 m. The water leaving the test section is collected in the drainage tank, which contains two drains at its bottom leading to the return pipe. An axial pump at the end of the return pipe discharges the water through a vertical perforated cylinder back into the settling chamber. The water tunnel also has a secondary pumping system that is used to circulate the water when the tunnel is not in use so that it can be filtered and chlorinated.

The upper surface of the water in the test section is covered with specially made panels to create a continuous upper boundary for the flow (Figure 3.2). These panels are made out of polyvinyl chloride (PVC) and are suspended above the test section from threaded rods at a height $h = 0.442$ m above the bottom wall. Each panel could be shifted horizontally relative to the adjacent panels to form a 25 mm gap that allowed the insertion of a probe from the top. A pair of small PVC pieces are used to cover the gap on either side of the probe. One of the panels is painted black to contain laser light inside the test section.

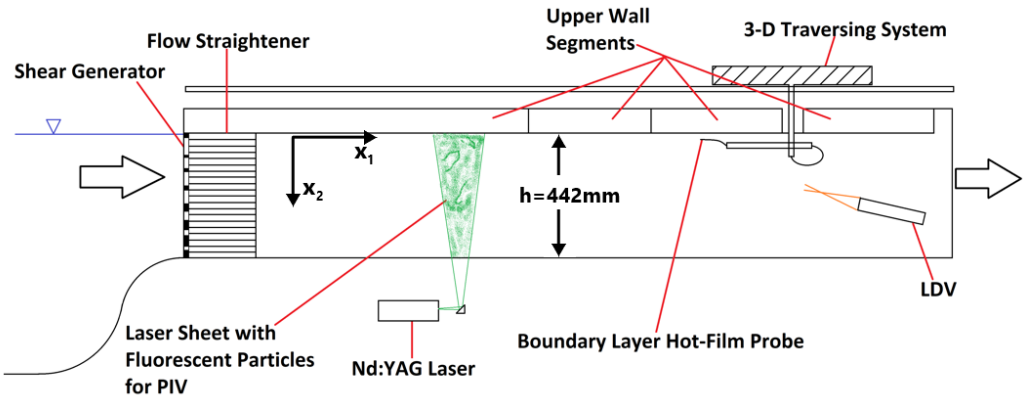

Figure 3.2: Schematic diagram of the water tunnel test section, also showing the instrumentation used.

The test section is equipped with four traversing systems, mounted along every face of the test section. Each of these traversing systems consists of two cylindrical rails on which run pillow blocks that support a carriage. The carriages traverse in

the streamwise direction but also contain secondary traverses that run vertically on the side traverses and horizontally on the top and bottom traverses, along directions normal to the streamwise direction.

3.2 Shear generator, flow separator and coordinate system definition

The shear generator, shown in Figure 3.3, is a perforated aluminum plate with a linear variation of its solidity (namely, the ratio of blocked and total areas). When flow passes through the plate, the variation of obstruction results in an approximately linear vertical velocity profile, which generates a uniformly sheared flow. The flow

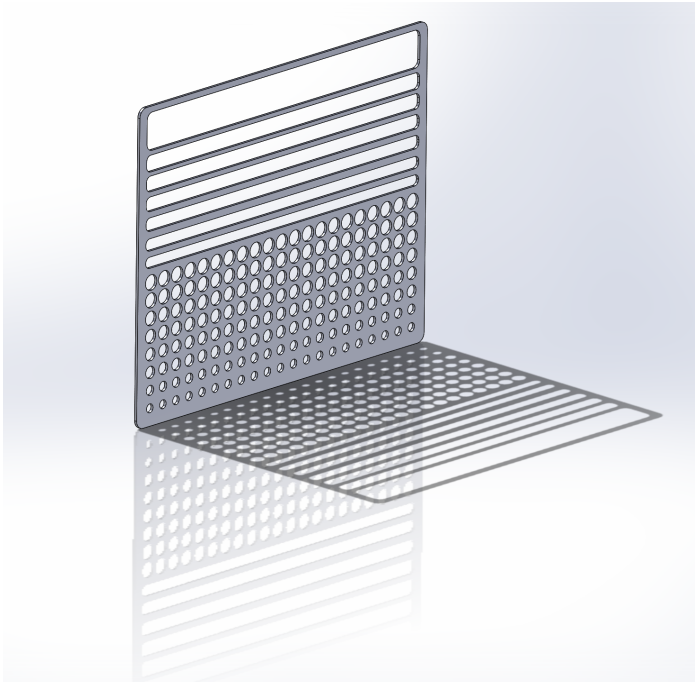

Figure 3.3: The shear generator.

separator, seen in Figure 3.4, consists of a PVC frame that supports thin glass plates, which separate the stream into parallel channels with equal heights, thus discharging fluid with a uniform length scale. The flow separator also acts as a flow straightener, which compensates for streamline displacement towards the higher speed region crated by the shear generator.

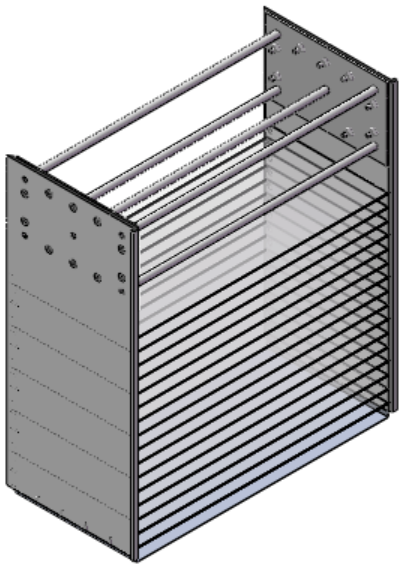

Figure 3.4: The flow separator.

The origin of the Cartesian coordinate system used in the present investigation is located on the vertical centreplane of the test section, at the bottom of the top panel and on the exit of the flow separator. The three axes x_1, x_2, x_3 will be referred to as, respectively, streamwise, transverse (or, occasionally, vertical) and spanwise (Figure 3.5).

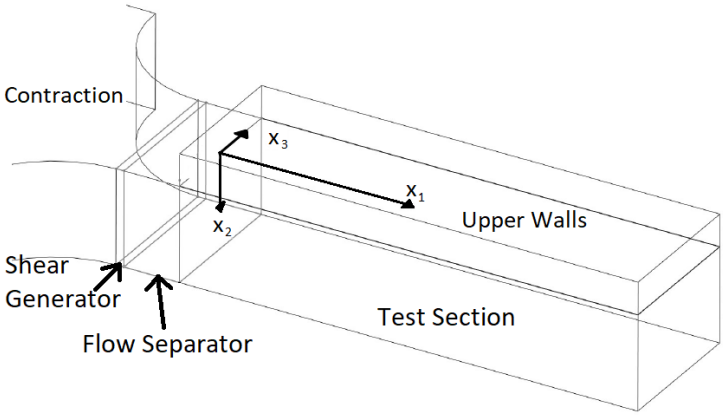

Figure 3.5: The coordinate system in the test section.

3.3 Laser Doppler velocimetry

Figure 3.6 depicts a simplified setup of a basic laser Doppler velocimetry (LDV) system, set up to measure one component of the flow velocity vector. The laser beam is split into two parallel beams using a transmitter, which, after passing through a converging lens, are made to intersect in a measurement volume, where they interfere with each other to form a group of dark and bright fringes. When a particle transported by the fluid passes through the measurement volume, it scatters light, which is captured by the laser head and is converted to an electric signal, called a burst, by a photo-detector. The burst is fluctuating at a frequency which is proportional to the local flow speed and is measured by a burst signal analyser (BSA). The presently

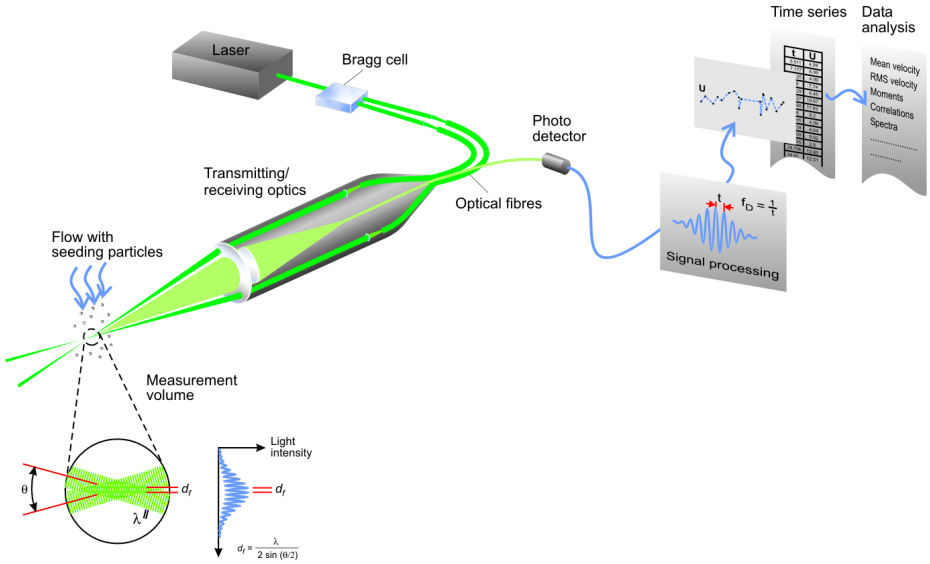

Figure 3.6: Schematic representation of the LDV measurement technique (reproduced with permission from Dantec Dynamics).

used LDV system was supplied by Dantec Dynamics (Skovlunde, Denmark) and was set up to measure simultaneously two velocity components, the streamwise and transverse ones. A laser beam, produced by a 5 Watt Argon-ion laser (Model # 95L-5, Lexel Laser, Fremont, USA), is split by the transmitter (Fibre Flow, Model # 60x41) to two pairs of beams. The wavelengths of light in the two pairs are, respectively, 488 nm and 514.5 nm. The transmitter is connected to the head with a fibre-optic cable. The two pairs of beams exit the head on two planes perpendicular to one another and

such that all beams are focused in the measuring volume. An optoacoustical device (Bragg cell) is used to shift the frequency of one beam in each pair by 40 MHz, which creates travelling interference fringe patterns, thus increasing the resolution of the system and allowing the measurement of zero and negative velocities. The lens used with the laser head has a focal length of 243 mm, which produces a measurement volume of $0.118 \times 0.118 \times 1.513$ mm in air. The particles used for the LDV measurements were fused borosilicate hollow glass beads (Potters Industries LLC, Valley Forge, USA), with a density of $1{,}100 \pm 50$ kg/m^3 and an average size of 10 μm.

3.4 Particle image velocimetry

Planar particle image velocimetry (PPIV, or simply PIV) provides a vector map of the velocity field on a plane area, rather than point values. The essential steps in this method are illustrated in Figure 3.7. The main components of the present system, which was manufactured by LaVision Inc. (Ypsilanti, USA) are a) a double pulsed laser system that produces two pulses of light (New Wave Research, Inc., Solo PIV 120XT) in the form of sheets, generated by a divergent sheet lens (LaVision #1108560) and separated by a very short time interval; b) a camera (LaVision Imager ProX 4M) with a lens (Nikon, Nikkor 50 mm f/1.8D), set up to record consecutively two images of a planar area illuminated by the pulses; and c) a timing mechanism (Lavision PTU-9 External #1108058) used to synchronise the laser and the camera. The same particles that were used for the LDV method were also serving as tracers for the PIV method. The frequency at which measurements were taken was 7.23 Hz. Each recorded image was split up into multiple small squares and correlations were performed between each pair of consecutive images, from which the local velocity was calculated.

3.5 Hot-film anemometry

Hot-film anemometry measures the flow velocity via its relationship with the convective cooling of an electrically heated sensor. A thin film of conductive material is deposited on a quartz fibre and is insulated electrically by a thin layer of quartz.

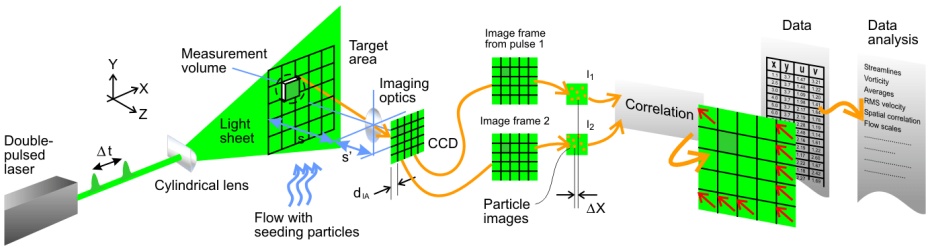

Figure 3.7: Schematic representation of the PIV measurement technique (reproduced with permission from Dantec Dynamics).

Current provided by a constant temperature circuit is run through the film and heats it to a specified temperature that is higher than that of the surrounding fluid. A voltage corresponding to the current required to maintain this film temperature is measured and the flow velocity is found by calibration. This voltage is discretised by a data acquisition system (DAS) and processed by a computer. A block diagram of a hot film anemometry system can be seen in Figure 3.8.

The hot-film probe used in this research was a Dantec 55R15 probe, which has a 2 μm nickel film on a quartz fibre that is 70 μm in diameter and 1.25 mm long. It is a boundary layer probe, which means that the prongs supporting the fibre were bent to offset the sensor, so that it can be positioned closer to the wall than the main probe body. The anemometer is an AA Labs AN-1002 unit and the DAS is a BNC-2110 model by National Instruments. The DAS is connected to the computer using a DAS to a peripheral component interconnect card provided by National Instruments.

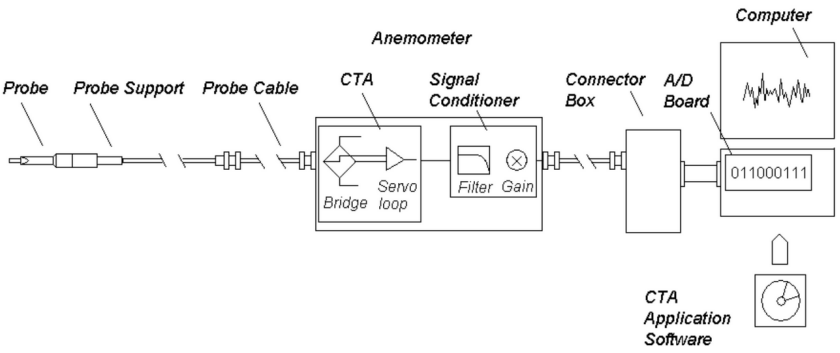

Figure 3.8: The process of hot-film anemometry (reproduced with permission from Dantec Dynamics).

Chapter 4

Experimental Procedures

This chapter describes the methods used to take measurements with laser Doppler velocimetry, particle image velocimetry and hot-film anemometry. It also elaborates on the method used to identify vortices in PIV velocity maps.

4.1 Laser Doppler velocimetry

The LDV head was mounted on the side of the test section on three stacked traverses, which allow traversing in three mutually perpendicular directions (Figure 4.1). Measurements were taken on the vertical centreplane of the test section ($x_3 = 0$). For turbulence measurements, the streamwise U_1 and vertical U_2 velocity components were measured in coincident burst mode, which considers a measurement valid if there is a burst in both directions simultaneously. To take measurements close to the upper wall (within 16 mm), the beams measuring the vertical component were blocked and only the streamwise component was measured. Measurements of each USF profile were made at 33 x_2 locations, at each of which 5000 samples were recorded over an average time of 140 s. For measurements near the edge of the boundary layer, 10000 samples were recorded over a time between 48 and 770 s (average of 235 s), which was at least 100 times greater than the local integral time scale. At the two streamwise positions of main interest, $x_1/h = 5.1$ and 6.5, additional one-dimensional measurements were taken that included at least 20000 samples and on average extended for over 360 s, as well as additional two-dimensional data that included 10000 samples and took 180 s on average.

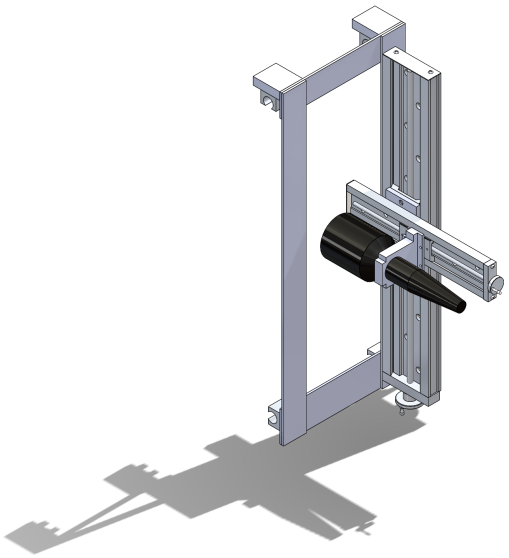

Figure 4.1: The LDV laser head mounted on the side traverse.

4.2 Particle image velocimetry

PIV images were taken in two planes of measurement, the vertical centreplane (x_1, x_2) and the horizontal plane (x_1, x_3). For the measurements in the vertical plane, the laser was positioned underneath the test section and the laser sheet was reflected upwards by a mirror (Figure 4.2). The camera was attached to the three-dimensional side traverse, which allowed the light sheet to be in focus regardless of its spanwise plane position (Figure 4.3). The size and location of the images were determined from images of a fine ruler that was inserted on the focal plane of the camera. To take measurements in the horizontal plane, the laser was positioned on the side of the test section, resting on wooden structures with different heights, and a mirror reflected the light sheet into the test section. The camera was setup on a tripod underneath the test section facing upwards.

Prior to determining the vector fields from image pairs, the image pairs were pre-processed. A sliding background was subtracted from the image with a scale between 256 and 512 pixels and the particle intensities were normalised with a scale between one and four pixels. An algorithmic mask was applied to remove any dead pixels in

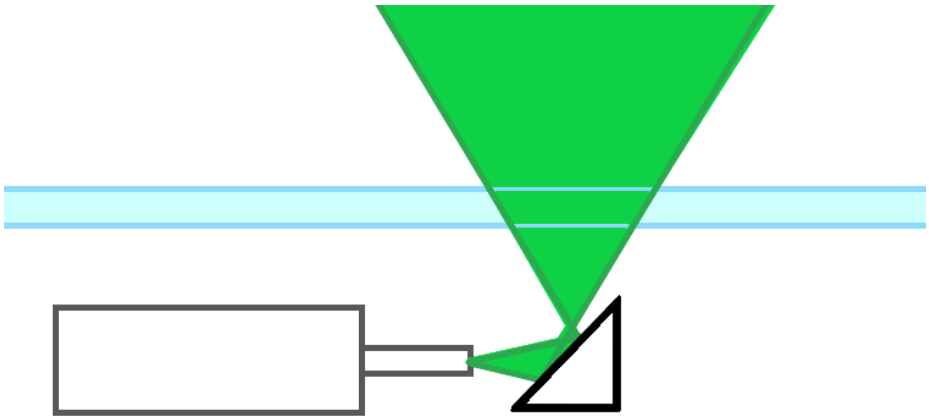

Figure 4.2: Sketch of the laser and the light sheet entering the test section either from the bottom or from a side wall.

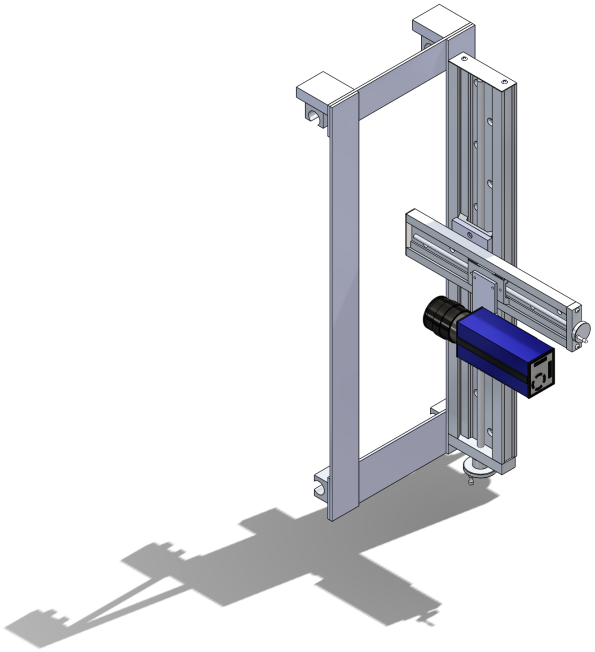

Figure 4.3: The PIV camera mounted on the side traverse.

the camera photodiode array or overexposed regions in the image. Each image was processed in an initial pass on 128×128 pixel squares with a 50% overlap and in a second pass on 32×32 pixel squares. A particle within the first image was matched with a particle in the second image of each pair and a correlation was computed for all particle pairs from which the local velocity magnitude was determined as the ratio of the particle displacement that corresponded to the maximum correlation and the time difference between the images. The direction of the velocity vector projection on the image plane was also determined. Post-processing consisted of deleting values that were significantly different from neighbouring ones and removing sections of the resulting vector field where the vector density was relatively low. Vectors that exceeded the range of expected velocity were also removed and replaced by interpolated values to fill-in sections of the vector field that were sparse. The edge regions of images were discarded to prevent the final results from being influenced by edge effects.

4.2.1 Vortex identification

The process of identifying vortices on PIV vector maps was the same as the one that has been described in detail by Vanderwel (2009). It is based on the swirling strength, a scalar parameter whose value distinguishes discrete vortices from a background flow with mean vorticity. A vortex was assumed to exist when the swirling strength exceeded a specified threshold value. Regions of the velocity map with sufficiently large swirling strength were fitted with an ellipse using a minimum volume ellipse function. The orientations of the ellipse axes were used to determine the orientation of the vortex axis. Counter-rotating vortex pairs were also identified with the use of another algorithm and were understood to be the legs of horseshoe-shaped vortices.

4.3 Hot-film anemometry

The hot-film probe was inserted in the test section from the top using waterproof parts. It was mounted on the upper traversing system and could be traversed in all three directions. The overall setup of the hot-film system can be seen in Figure 4.4. The hot-film signal was sampled at a rate of 800 Hz over a 35 s interval, which is

approximately 100 times the typical integral time scale. Ensemble averaging was performed over 20 of these records at each location. The hot-film signal was low-pass filtered by two double-pole low-pass filters in series with the first filter cut-off frequency set to 380 Hz and the second one set to 1.4 kHz. After the voltage signal was recorded and corrected for temperature differences, it was further low-pass filtered by a digital filter with a cut-off frequency that was 2.1 times the Kolmogorov frequency to prevent aliasing.

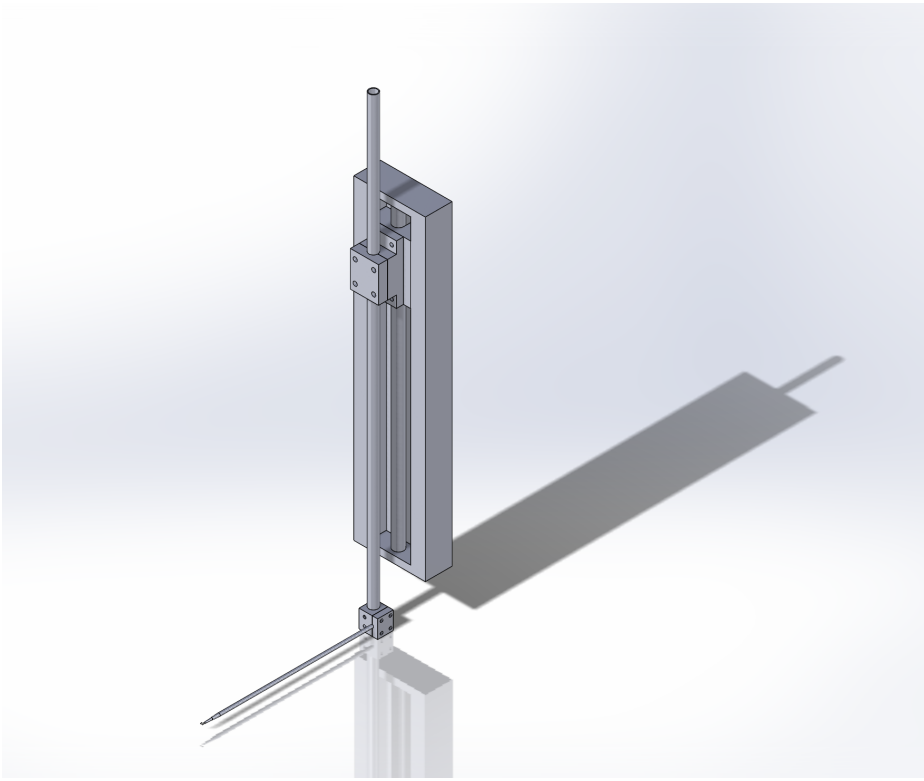

Figure 4.4: The hot-film probe mounted on the upper traverse.

A hot-film probe, in principle, is capable of measuring the flow velocity at a higher sampling rate than is possible with an LDV system. This would be necessary for measuring the temporal derivative of the velocity, from which one can estimate the Taylor microscale and the dissipation rate. The usual procedure for measuring flow velocity with hot-wire and hot-film anemometers is to calibrate the probe by recording its voltage for a range of velocities that are measured by some other method. In this work, calibration was performed several times *in situ vs.* LDV measurements.

Unfortunately, such calibrations proved to be unusable, due to the observed significant and non-repeatable signal drift of the hot-film. Monitoring the hot-film signal over many hours did not show any repeatable trend, but showed fluctuations or monotonic drifts by amounts that were sometimes as large as 60 mV/hr. Drift of hot-films immersed in water is well known to users, but there is no effective way to eliminate it or correct for it.

Although its source remains unclear, it is possibly related to changes in the thermal resistance of the hot-film surface, as a result of deposits on this surface, which may build up or be removed by the stream. Following the manufacturer's suggestions and our personal intuition, we cleaned the hot-film using a small brush and vinegar, replaced the water inside the test section and increased electric conductivity of water by adding sodium calcite, but any improvement that occurred was short-lived. Thus, the hot-film measurements were unsuitable for measuring the mean velocity, the streamwise turbulent stress or the streamwise component of the dissipation rate, from which the total dissipation rate can be estimated under the assumption of local isotropy. Fortunately, we devised a procedure by which we could measure directly the Taylor microscale from the hot-film signal, even in the presence of drift.

First, let us assume that there is no voltage drift and so both the flow velocity and the hot-film signal are stationary. The instantaneous hot-film voltage E is customarily related to the flow velocity U_1 by the modified King's law

$$E^2 = A + BU_1^n \ , \tag{4.1}$$

where A, B, n are calibration constants and n is typically around 0.45. This is a non-linear relationship and so, the voltage fluctuation, e, would not be exactly proportional to the velocity fluctuation, u_1. For example, a Gaussian velocity distribution would produce a skewed voltage distribution. Nevertheless, if velocity fluctuations are sufficiently small, one may approximate Equation (4.1) by the local tangent and one would get

$$e \approx \alpha u_1 \ , \tag{4.2}$$

where the value of the proportionality coefficient

$$\alpha = \frac{dE}{dU_1} \ , \tag{4.3}$$

would vary across the flow as U_1 changes. In the presence of voltage drift, one would expect that the calibration constants would change as well and so, in general, α would depend on both U_1 and E in an unpredictable fashion. A change δu_1 of velocity over a small time interval δt would produce a change of voltage $\delta e \approx \alpha \delta u_1$, from which one can deduce that

$$\frac{de}{dt} \approx \alpha \frac{du_1}{dt} \ . \tag{4.4}$$

Under the assumption of Taylor's frozen flow approximation, which is satisfied by the present flow, one gets

$$\frac{\partial u_1}{\partial x_1} \approx -\frac{1}{\overline{U}_1} \frac{du_1}{dt} \ . \tag{4.5}$$

With the use of these expressions, one can determine the Taylor microscale from the hot-film voltage as

$$\lambda = \frac{{u_1}'}{\sqrt{\overline{(\frac{\partial u_1}{\partial x_1})^2}}} \approx \overline{U}_1 \frac{{u_1}'}{\sqrt{\overline{(\frac{du_1}{dt})^2}}} \approx \overline{U}_1 \frac{e'/\alpha}{\frac{1}{\alpha}\sqrt{\overline{(\frac{de}{dt})^2}}} \approx \overline{U}_1 \frac{e'}{\sqrt{\overline{(\frac{de}{dt})^2}}} \ . \tag{4.6}$$

In this expression, the mean velocity $\overline{U}_1$ can be specified from the LDV measurements. Equation (4.6) is only valid under two assumptions: first that the velocity fluctuations are small compared to the mean local velocity and second that the time interval of samples from which the Taylor microscale was determined was sufficiently short for voltage drift to be negligible. Both assumptions were satisfied fairly well by the present conditions. First, the turbulence intensity $u_1'/\overline{U}_1$ in most of the flow domain of interest ($0.5 \leq x_2/\delta \leq 2.5$) was in the range 2 to 6%, which is deemed to be sufficiently small for non-linearity effects not to be significant. Second, each hot-film data block extended over 35 s, during which voltage drift would be at most of the order of 0.5 mV and so its effect on α is not expected to be significant either.

On a final note, $\overline{(\frac{de}{dt})^2}$ was calculated by extrapolation of $\overline{(\frac{\delta e}{\delta t})^2}$ to zero δt, as shown in Figure 4.5.

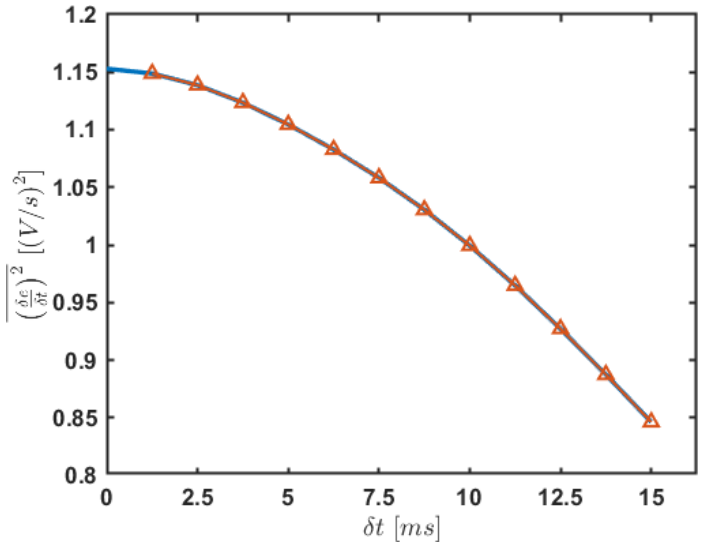

Figure 4.5: Representative calculation of the time derivative variance of the voltage.

Chapter 5

Results and Discussion

This chapter presents the results of this research. Measurements obtained with the LDV system include the local mean velocity, the streamwise and transverse Reynolds stresses and the shear stress correlation coefficient. Measurements obtained with the hot-film probe include the integral length scale and the Taylor microscale. Finally, this chapter presents the measured properties of coherent structures, identified from velocity maps obtained with the PIV system.

5.1 The USF as a free stream

Mean velocity profiles, measured at different streamwise locations in order to demonstrate that the free stream was indeed a USF, are shown in Figure 5.1. As the TBL evolved streamwise, it encroached into the USF, altering the USF mean profile in an increasingly larger region. The mean shear remained approximately constant ($d\overline{U}_1/dx_2 \approx 0.41$ s^{-1}) in the undisturbed part of the USF for $x_1/h \geq 1.4$ (Figure 5.2). The shear parameter, based on an average centreline velocity $\overline{U}_{1c} \approx 0.13$m/s at $x_2/h = 0.5$, was $\beta = (1/\overline{U}_{1c})(d\overline{U}_1/dx_2) \approx 2.9$ s^{-1}. Figure 5.3, which shows profiles of the standard deviation of the streamwise velocity at different streamwise locations, demonstrates that the turbulence in the USF was approximately homogeneous on a transverse plane. The level of inhomogeneity of this flow was comparable to those observed in previous USF studies by Vanderwel (2009) and Kislich-Lemyre (2003). Moreover, as Figure 5.4 demonstrates, the streamwise Reynolds stress generated by the flow separator decayed in the region $x_1/h \leq 4$, but this parameter grew exponentially further downstream, following the well-established (Vanderwel, 2009) USF exponential growth law $\overline{u_1^2}/\overline{U}_{1c}^2 \propto e^{0.1\beta x_1}$. In summary, the present results indicate that the free stream was a conventional USF, and so one may use previous findings about its structure.

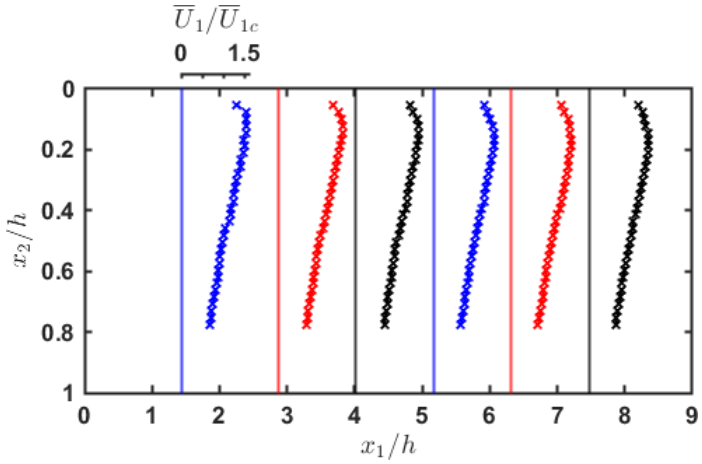

Figure 5.1: Streamwise evolution of the mean velocity profiles demonstrating the uniformity of mean shear in the free stream; vertical lines indicate the origin of the corresponding profile.

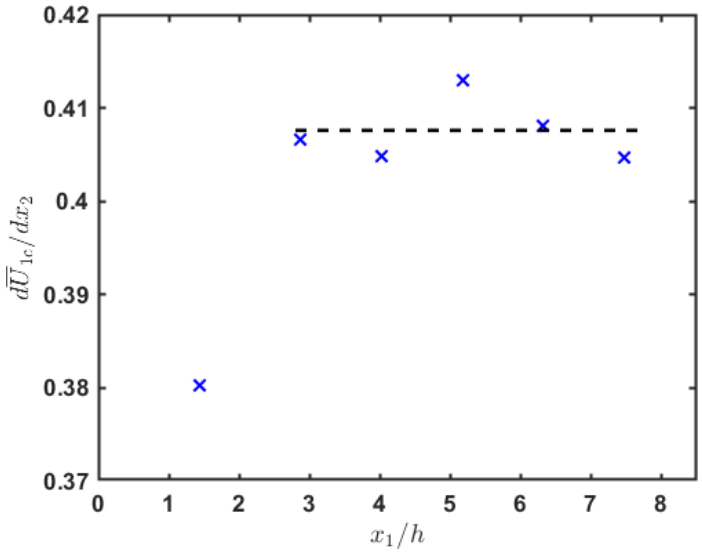

Figure 5.2: Streamwise evolution of the mean shear.

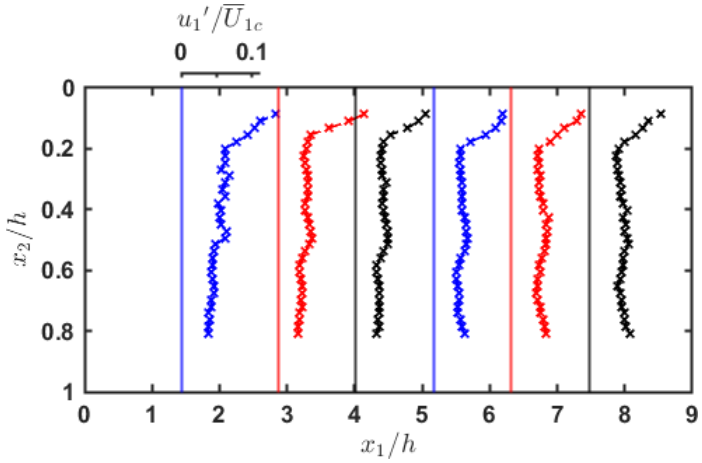

Figure 5.3: Streamwise evolution of the streamwise velocity standard deviation; vertical lines indicate the origin of the corresponding profile.

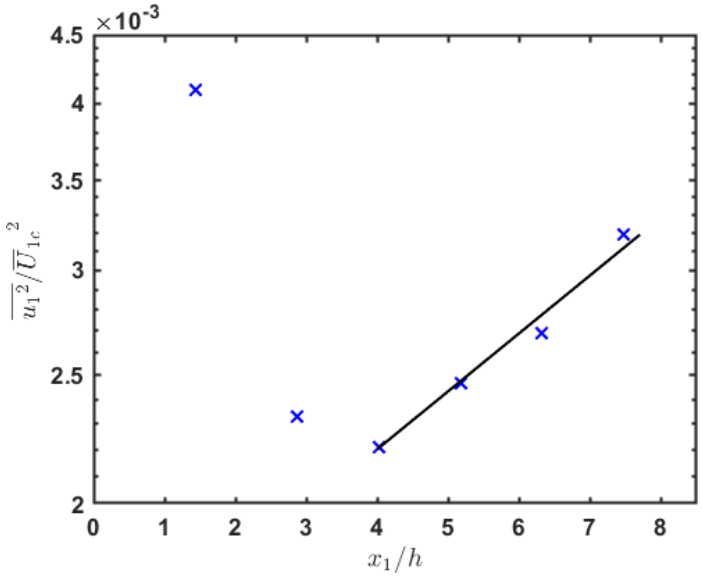

Figure 5.4: Streamwise evolution of the centreline streamwise Reynolds stress, also showing the exponential growth law $\overline{u_1^2}/\overline{U}_{1c}^2 \propto e^{0.1\beta x_1}$, fitted to the values in the region $4 \leq x_1/h \leq 7.5$.

5.2 Mean streamwise velocity profiles

Mean streamwise velocity profiles, measured with the one-dimensional LDV system, are shown in Figure 5.5.

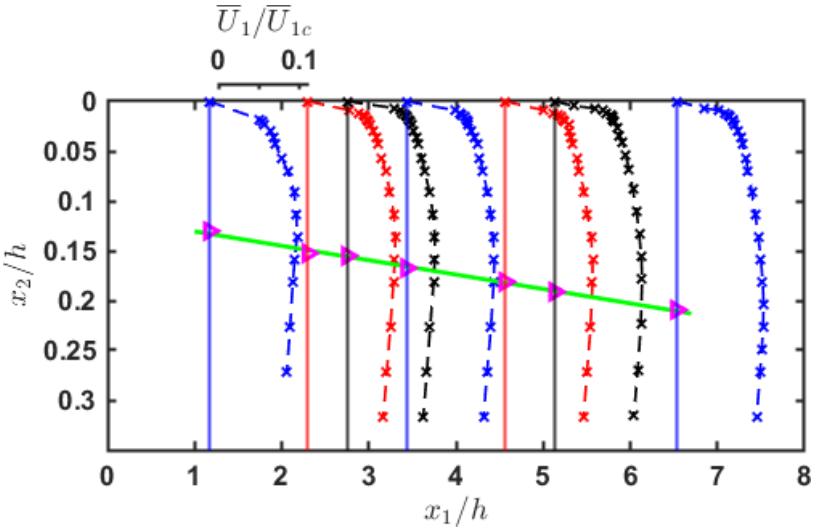

Figure 5.5: Streamwise evolution of the mean velocity profiles near the wall.

High-order polynomials were fitted to the data in sections of each profile, which were used to determine the maximum velocity $\overline{U}_{1max}$ and the distance δ of the maximum velocity location from the wall, considered to be the boundary layer thickness. When plotted *vs.* x_2/δ (Figure 5.6), most mean velocity profiles nearly collapsed, showing a fair degree of self-similarity of the outer boundary layer. The notable exception was the profile that was closest to the origin ($x_1/h = 1.17$), which was not as developed as the others. Moreover, and although not visible in this figure, the farthest away ($x_1/h = 6.5$) profile was also slightly different from the others, which may indicate that other influences in the test section were starting to build up. None of the profiles was represented accurately by the canonical 1/7th power law (also plotted in the figure) or any other power law. Somewhat surprisingly, the difference between the two profiles is relatively large only in the inner TBL.

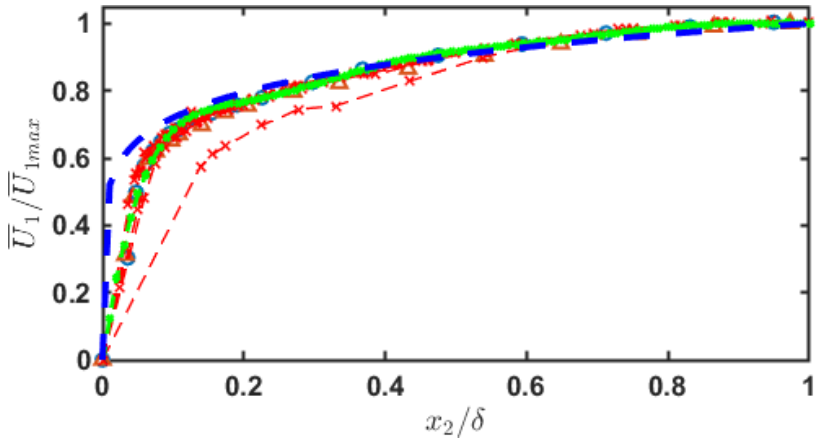

Figure 5.6: Normalised mean velocity profiles at all streamwise locations *vs.* the normalised distance from the wall; × measurements and - - - fitted polynomial at $x_1/h = 1.17$; measurements at all other locations nearly collapse and were collectively fit by an eighth order polynomial (—); – – – 1/7th power law.

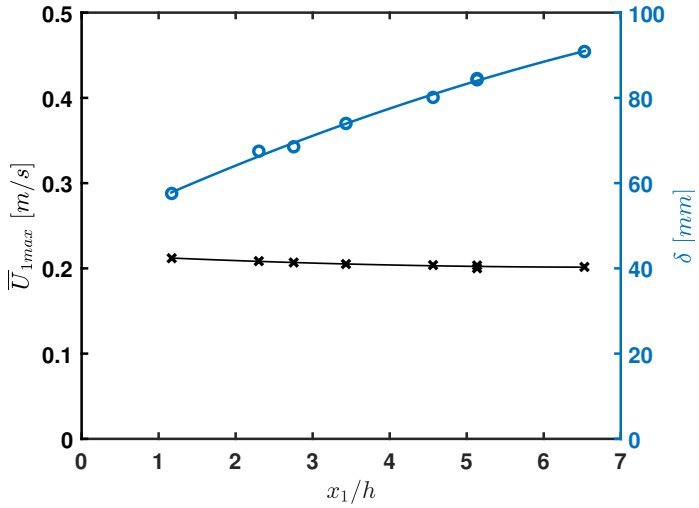

Figure 5.7: The streamwise evolution of the maximum velocity and the boundary layer thickness, also showing the power law fitted to the latter.

The values of $\overline{U}_{1\text{max}}$ along the test section are shown in Figure 5.7. It is interesting to note that $\overline{U}_{1\text{max}}$ remained nearly constant along the test section. An explanation for this observation is as follows. The decrease of $\overline{U}_{1\text{max}}$ that would be ideally caused by the encroachment of the TBL into an otherwise unbounded USF is counteracted by acceleration of flow in the core of the test section, which compensates for the flow velocity decrease in all boundary layers surrounding the USF in the water tunnel.

As a result of the near constancy of $\overline{U}_{1\max}$, the TBL Reynolds number Re_x grew essentially linearly with streamwise distance, as shown in Figure 5.8.

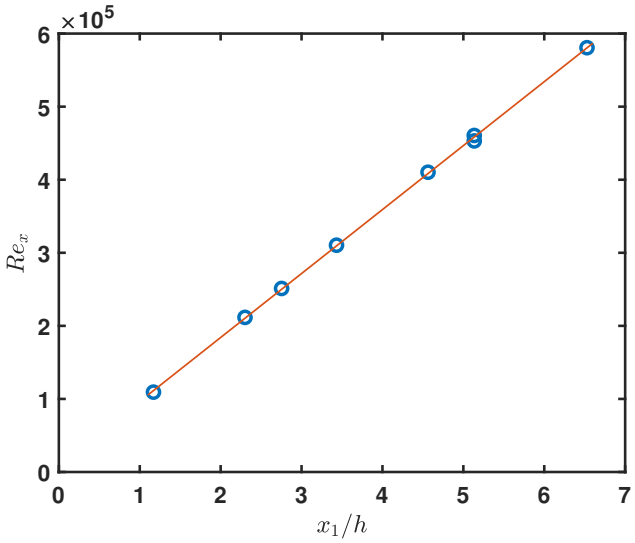

Figure 5.8: The streamwise evolution of Re_x.

As also shown in Figure 5.7, the physical boundary layer thickness increased monotonically with streamwise distance and could be fitted well by the power law $\delta/h \approx 0.029(x_1/h + 5.4)^{0.8}$. It is interesting to note that the exponent of this power law matches the value of canonical TBL with a laminar, uniform free stream. The inclusion of an effective origin that was upstream of the exit plane of the flow separator was necessary to account for the fact that the present boundary layer did not start with a zero thickness at that location, but with a significantly wall-affected profile. The boundary layer thickness Reynolds number, shown in Figure 5.9, was described well by the power law $\mathrm{Re}_\delta \approx 2600(x_1/h + 5.7)^{0.8}$.

Integration of each mean velocity profile in the region $0 < x_2 \leq \delta$ provided the momentum integral thickness θ. An example of polynomial fitting and momentum integral thickness calculation is shown in Figure 5.10. The directly calculated ratio θ/δ is shown in Figure 5.11. Excluding the two values at the two ends of the measurement range, this parameter was on the average 0.0924, which is only slightly lower than the canonical value of 0.094, despite the difference between the present mean profile and the canonical 1/7th power law in the inner part of the TBL. For rough purposes, and with some reservation for the furthest downstream location, one may approximate

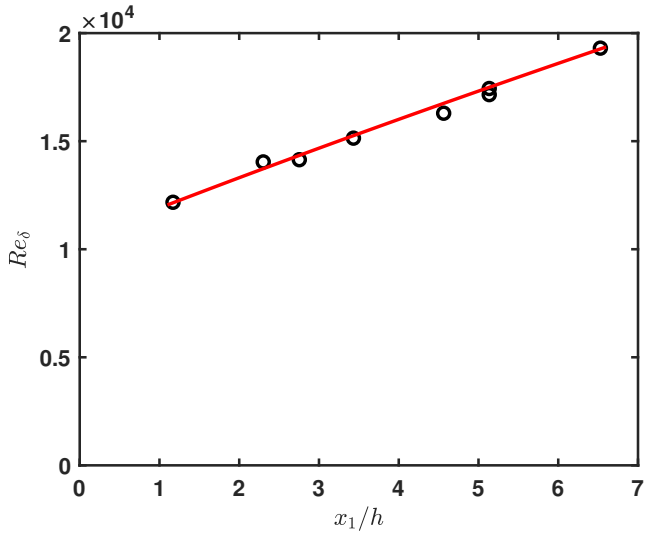

Figure 5.9: The streamwise evolution of the boundary layer thickness Reynolds number; fitted line is the power law $\mathrm{Re}_\delta \approx 2600(x_1/h + 5.7)^{0.8}$.

the momentum thickness Reynolds number as $\mathrm{Re}_\theta \approx 240(x_1/h + 5.7)^{0.8}$. The directly measured values of Re_θ and the power law describing the ideal momentum thickness Reynolds number are presented in Figure 5.12.

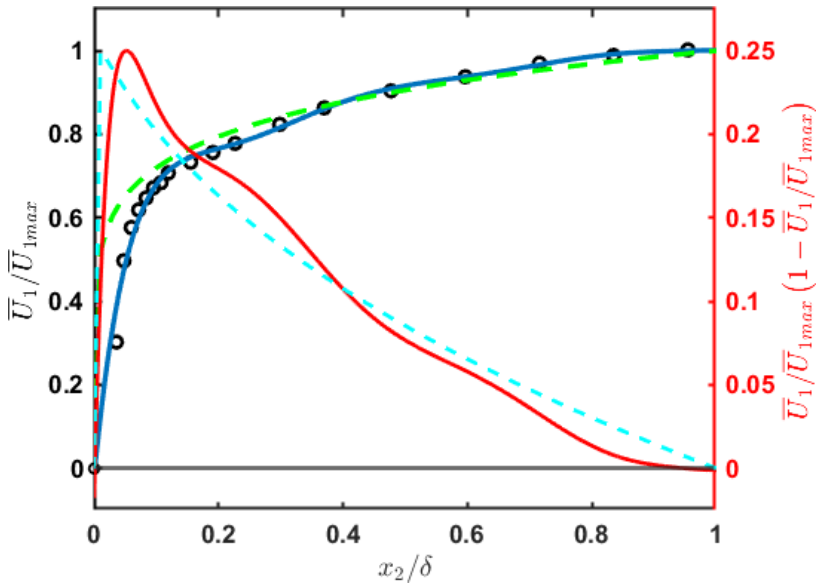

Figure 5.10: Example of polynomial fitting (—) to mean velocity data (∘) and integrand for the momentum integral thickness calculation (—); the 1/7th law (– – –) and the corresponding integrand (–) are also shown for comparison.

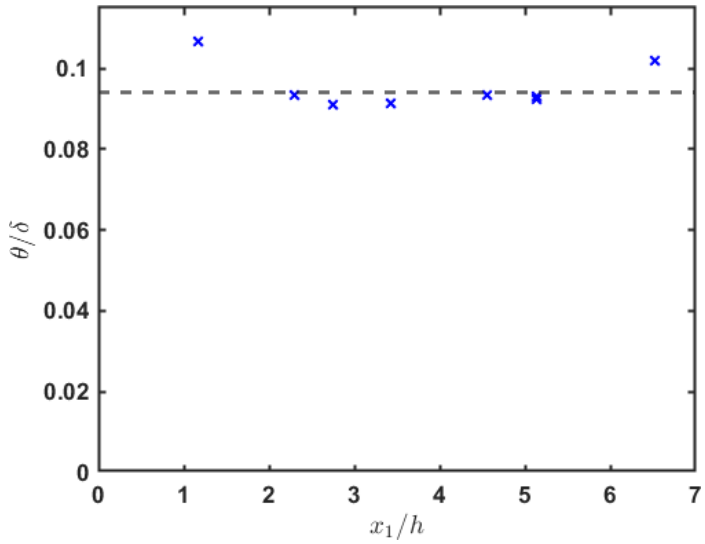

Figure 5.11: The streamwise evolution of the ratio θ/δ, also showing its value in canonical TBL (– – –).

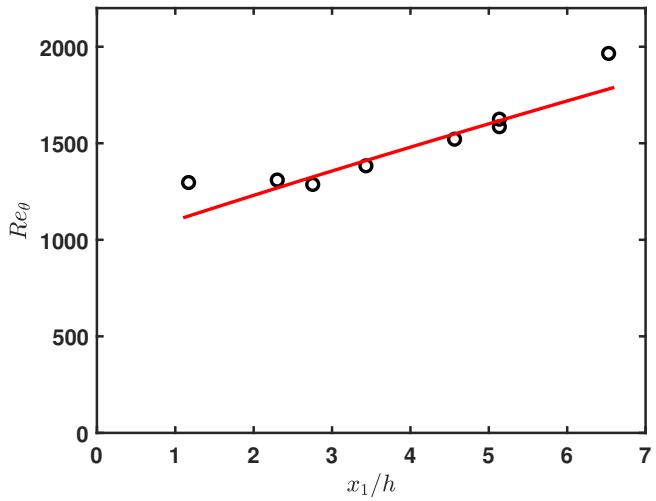

Figure 5.12: The streamwise evolution of Re_θ; — $240(x_1/h + 5.7)^{0.8}$.

5.3 Turbulent stresses

The velocity measurements presented in this section were more closely spaced and extended over longer intervals than those presented in previous sections, so that they are expected to have a lower uncertainty. Such measurements were collected only at two streamwise stations, corresponding to $x_1/h = 5.1$ and 6.5. One is cautioned,

however, that small changes in the flow characteristics may have occurred between sets of data taken at significantly different times because of the limited distance which could be traversed in one movement as well as the limited amount of time within a day.

The mean velocity profiles are presented in Figure 5.13 to serve as reference for the turbulence data. The normalised velocity profiles at the two streamwise stations are close to each other but do not collapse. Although the values of $\overline{U}_{1max}$ at the two stations were very close to each other, the boundary layer thickness δ was 10% larger in the downstream station than in the upstream one. As a result, locations with the same x_2/δ were closer to the wall for the upstream profile than the downstream one and thus had somewhat larger velocity.

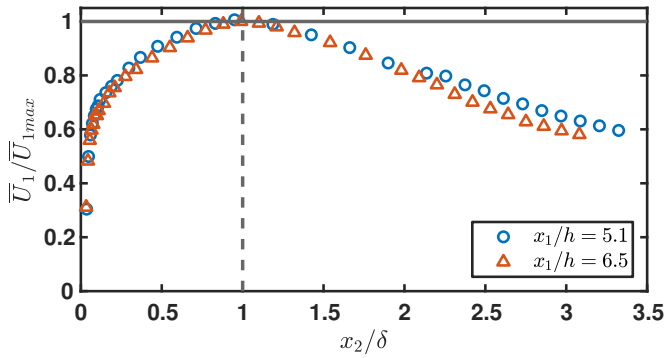

Figure 5.13: The normalised mean velocity at two stations on the test section centre-plane *vs.* the normalised distance from the wall.

The normalised standard deviations of the streamwise and transverse velocity components are, respectively, plotted *vs.* the dimensionless distance from the wall in Figures 5.14 and 5.15. The corresponding values at the two stations are quite close to each other, although they do not entirely collapse. Within the TBL ($x_2/\delta < 1$), both parameters generally increase towards the wall. It is noted that the 2D LDV system could not resolve the inner boundary layer, whereas the 1D LDV system could only resolve the edge of this region. Outside the TBL ($x_2/\delta > 1$), the turbulence was

roughly homogeneous.

The ratio u_2'/u_1', plotted in Figure 5.16, fluctuated around the canonical value of about 0.65 both within the USF and the TBL away from the edge. Near the edge ($x_1/\delta = 1$), however, this ratio took values closer to 1, which implies that this is a region of lower anisotropy, as expected considering that the mean shear vanishes at the edge.

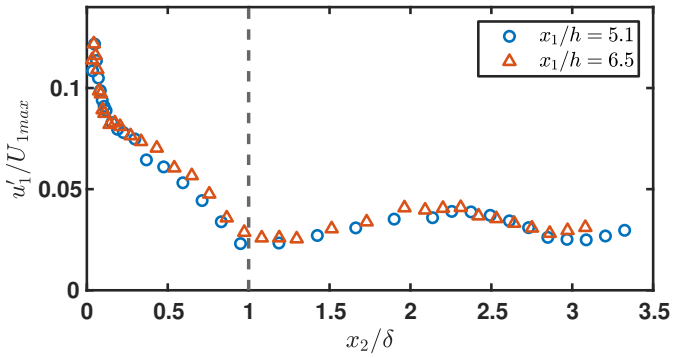

Figure 5.14: The normalised streamwise velocity standard deviation *vs.* the normalised distance from the wall.

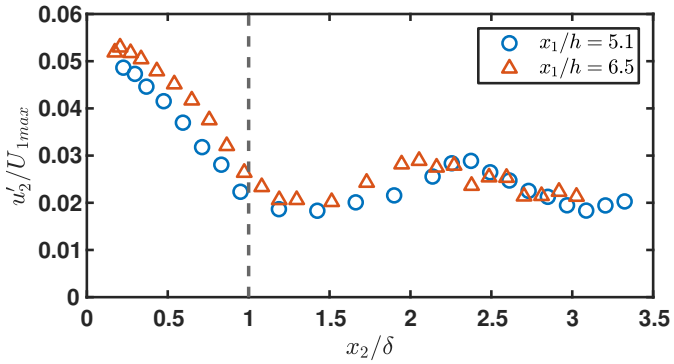

Figure 5.15: The normalised transverse velocity standard deviation *vs.* the normalised distance from the wall.

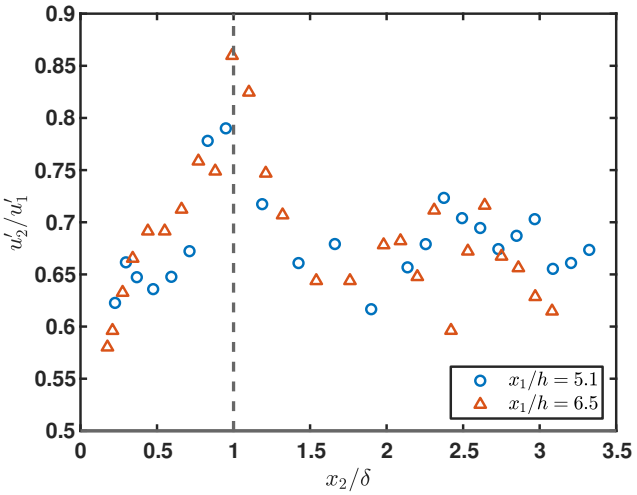

Figure 5.16: Ratio of the standard deviations of the transverse and streamwise velocity components *vs.* the normalised distance from the wall.

Finally, Figure 5.17 shows the shear stress correlation coefficient. In conformity with gradient transport, this parameter nearly vanishes at the TBL edge, where it changes sign so that it always has a sign that is opposite to that of the mean shear. Away from the edge, on both the USF and the TBL, its magnitude reaches the canonical value of about 0.4.

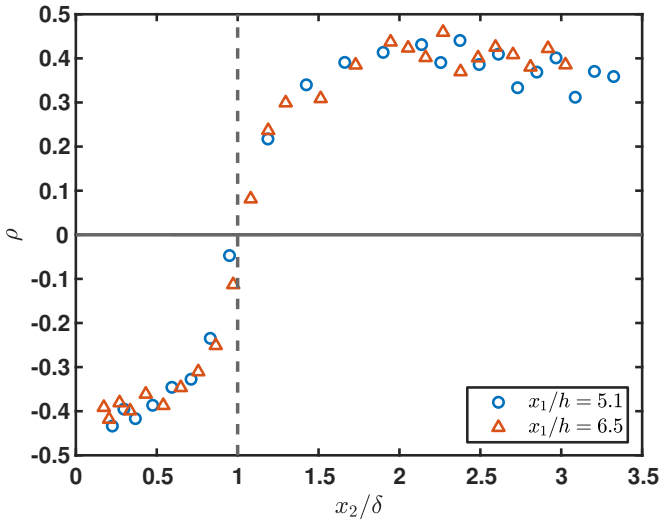

Figure 5.17: The shear stress correlation coefficient *vs.* the normalised distance from the wall.

In summary, the mean velocity and turbulence measurements show clearly that,

at some distance on both sides of the TBL edge, the flows are essentially canonical and are subjected to strong mean shear, which produces a strong turbulent shear stress. In contrast, the near-edge region has low mean shear and shear stress and one would anticipate that the turbulence structure in this region would not be canonical; in other words, this flow would be multi-structure.

5.4 Length scales and energy dissipation rate

The streamwise integral length scale L was computed as $L = \overline{U}_1 T$, where the integral time scale T was determined by integrating the temporal auto-correlation coefficient of the hot-film voltage and the local mean velocity $\overline{U}_1$ was measured with the LDV system. As can be seen in Figure 5.18, L maintained values in the vicinity of 0.5δ in most of the flow region and decreased monotonically towards zero in the near-wall region ($x_2/\delta < 0.2$).

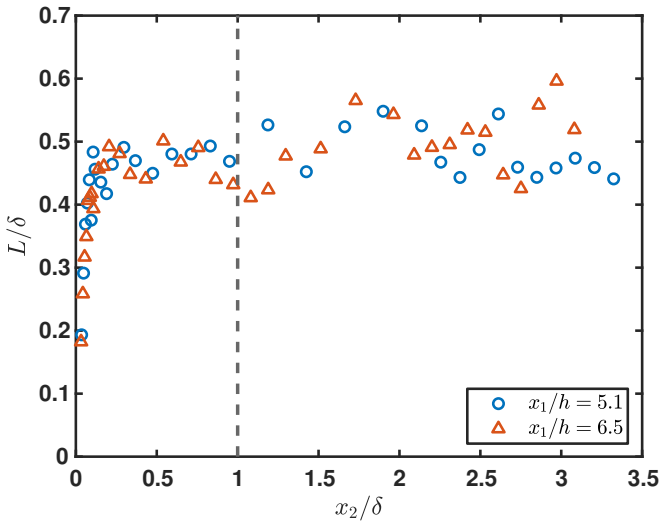

Figure 5.18: The integral length scale *vs.* the normalised distance from the wall.

The Taylor microscale, measured according to Equation (4.6), is shown in Figure 5.19. The results at the two streamwise stations are qualitatively consistent, although they do not collapse. When viewing these results, one must keep in mind that the USF is not perfectly homogeneous and that the measurement of λ is subjected to considerable uncertainty, which is hard to estimate, but is likely to be in the range 10-15%. At both locations and starting from the wall, λ increases with

distance up to $x_2/\delta \approx 0.8$, then it has a local minimum in the vicinity of $x_2/\delta = 1$ and finally increases to reach a nearly constant value in the USF. The local minima of λ/δ at the two stations do not coincide when plotted *vs.* x_2/δ, but it is interesting to note that they nearly do when plotted *vs.* x_2.

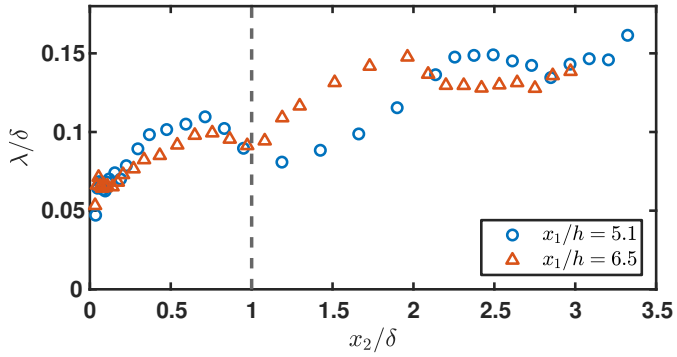

Figure 5.19: The Taylor microscale *vs.* the normalised distance from the wall.

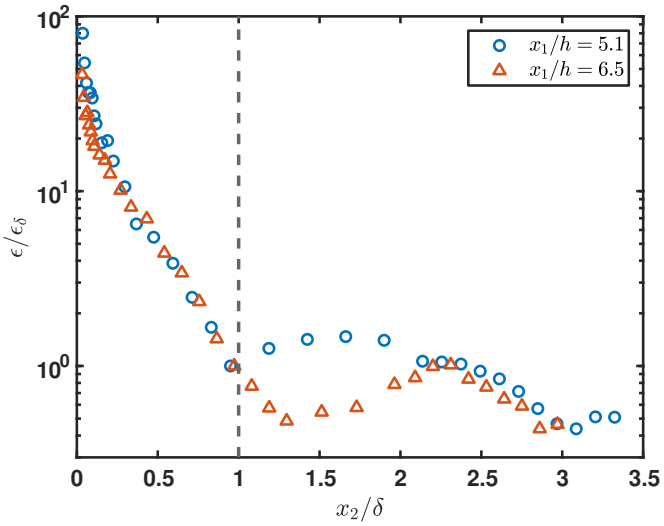

Figure 5.20: The energy dissipation rate, normalised by the edge values $\epsilon_\delta = 5.45$ and 6.80 m^2/s at $x_1 = 5.1$ and 6.5, respectively, *vs.* the normalised distance from the wall.

The rate of dissipation, computed with the use of Equation (2.9), is plotted in

Figure 5.20. This property takes its largest values near the wall and decreases monotonically across to the TBL towards its edge. It reaches a local minimum in the vicinity of the edge (multi-structure region) and then increases somewhat, decreases again and eventually seems to settle in the USF.

The Kolmogorov microscale η, computed from Equation (2.7),is shown in Figure 5.21. It is smallest near the wall, it increases across the TBL to reach a local maximum near the TBL edge, it decreases somewhat in the multi-structure region and then it increases again towards the USF.

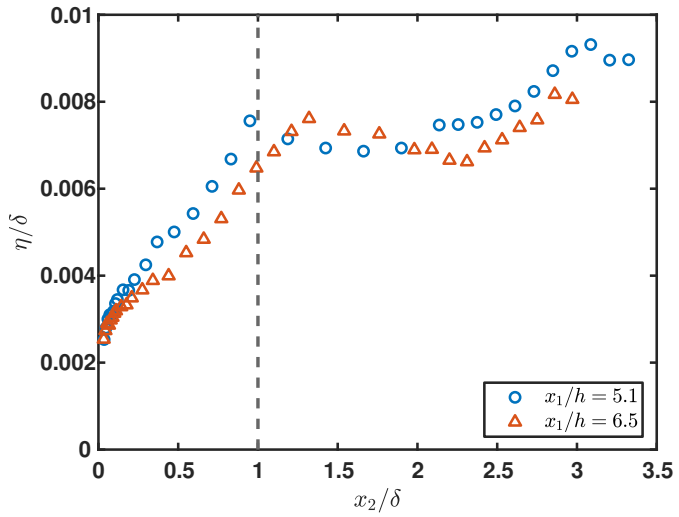

Figure 5.21: The Kolmogorov microscale *vs.* the normalised distance from the wall.

Figure 5.22 presents the length scale ratios λ/L and η/L. This figure demonstrates that the Kolmogorov length scale was separated from the integral length scale by two orders of magnitude, which is deemed to be sufficient for the formation of an energy cascade.

5.5 The dissipation parameter and the turbulence Reynolds number

Figure 5.23 shows profiles of the dissipation parameter at two streamwise stations. The appearances of the two profiles agree qualitatively with maxima occurring near the TBL edge at both stations, albeit with maximum values larger in the upstream station by a factor of roughly two. An important observation in this figure is that, away from the wall ($x_2/\delta \lesssim 0.5$ and $2 \lesssim x_2/\delta$), the present C_ϵ nearly matched

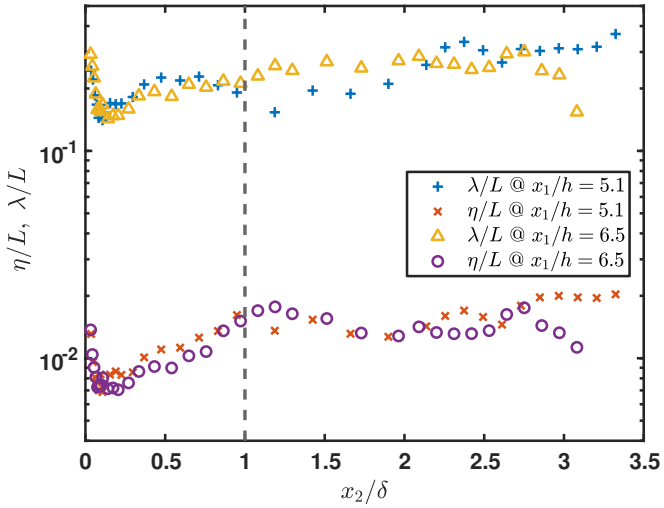

Figure 5.22: The ratios of Kolmogorov and Taylor microscales to the integral length scale *vs.* the normalised distance from the wall.

measurements in the TBL (Nedić et al., 2017) and the USF (Nedić and Tavoularis, 2016). In contrast, the present values at both stations are significantly larger than the corresponding values in the TBL and the USF. This observation qualifies the region $0.5 \lesssim x_2/\delta \lesssim 2$ as multi-structure turbulence. The data also seem to indicate that the multi-structure character and width of this region decrease from $x_1/h = 5.1$ to 6.5.

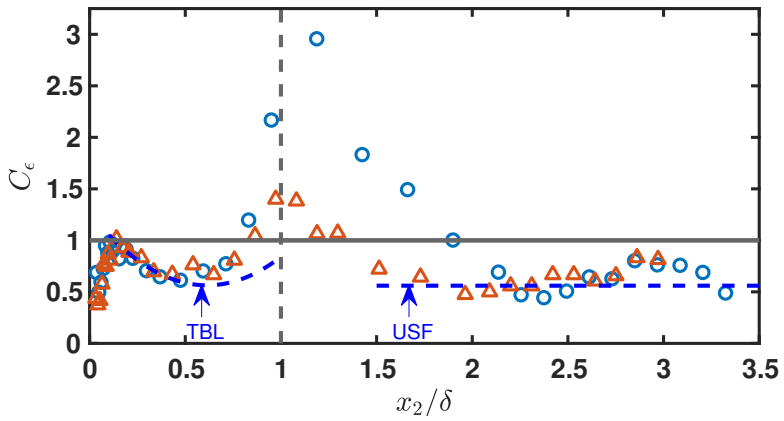

Figure 5.23: The dissipation parameter at $x_1/h = 5.1$ (○) and 6.5 (△) *vs.* the normalised distance from the wall; lines fitted to measurements of this parameter in a canonical TBL (Nedić et al., 2017) and a USF (Nedić and Tavoularis, 2016) are also shown.

The turbulence Reynolds number Re_λ across the flow at two streamwise stations is plotted in Figure 5.24. At both stations, the multi-structure region is characterised by the presence of a strong local minimum near the TBL edge. The intensity and width of this region diminish somewhat with streamwise distance, in conformity with the observation made for C_ϵ.

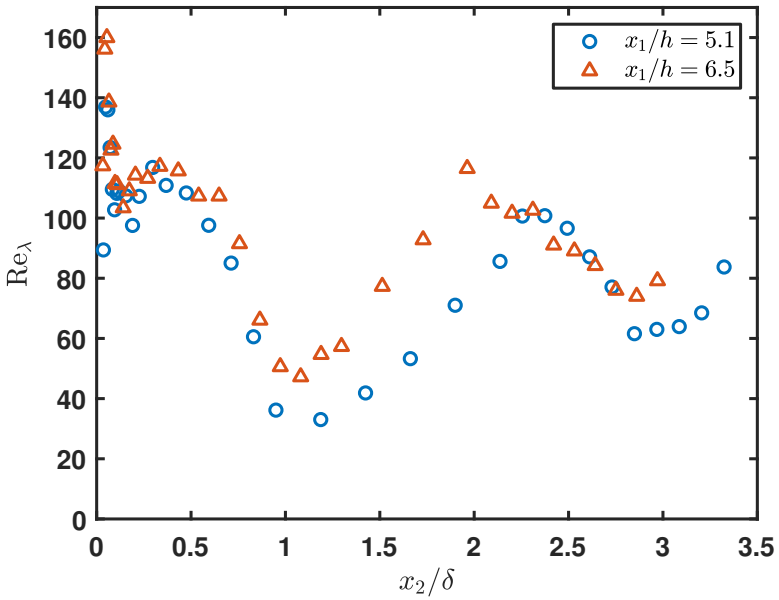

Figure 5.24: Re_λ *vs.* the normalised distance from the wall.

A comparison of Figures 5.23 and 5.24 demonstrates that, within the multi-structure region ($0.5 \lesssim x_2/\delta \lesssim 2$), the dissipation parameter and the turbulence Reynolds number have inverse profiles and so they are negatively correlated. The existence of an inverse relationship of the type $C_\epsilon \propto \mathrm{Re}_\lambda{}^{-1}$ is shown clearly in Figure 5.25. This relationship applies fairly well to the data at both stations, but the proportionality coefficients are somewhat different. The near-wall data ($x_2/\delta < 0.5$) did not show any apparent correlation between C_ϵ and Re_λ, but an inverse relationship was also roughly visible in the limited range of quasi-USF data $2 \lesssim x_2/\delta \lesssim 3.3$. It hardly seems a coincidence that the inverse relationship between C_ϵ and Re_λ in the present multi-structure region also holds for the near-grid region of grid-generated turbulence (Vassilicos, 2015) and for the multi-structure region of a USF distorted by

a grid (Nedić and Tavoularis, 2018). This issue fully deserves a theoretical investigation.

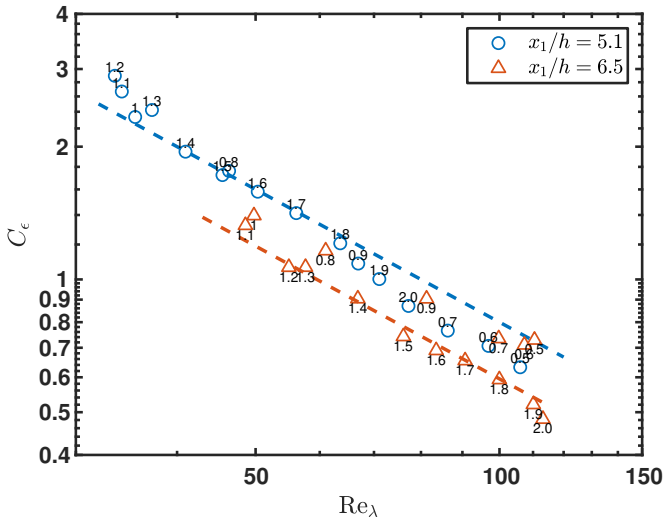

Figure 5.25: The dissipation parameter *vs.* the turbulence Reynolds number in the multi-structure region ($0.5 \lesssim x_2/\delta \lesssim 2$); the numbers next to the symbols are equal to the normalised distance from the wall, whereas the lines represent inverse relationships between these variables ($C_\epsilon \propto \mathrm{Re}_\lambda{}^{-1}$).

5.6 Comparisons with measurements in a boundary layer with a uniform free stream

The profiles of the mean velocity and the streamwise Reynolds stress across a TBL on the upper wall in the present water tunnel in the absence of USF were measured at $x_1/h = 5.1$ with the LDV system after the shear generator and flow separator were removed, but with the upper wall remaining in place. Table 5.1 lists the values of some basic properties of this boundary layer, as well as the corresponding values of the boundary layer in the presence of USF at the same streamwise location.

The normalised mean velocity profiles in the two flows are plotted together in Figure 5.26, which clearly shows that the free streams in the two cases were essentially uniform and uniformly sheared. The same two mean velocity profiles, but this time only inside the two boundary layers, are shown in Figure 5.27. Differences between the two profiles appear to fall within the measurement uncertainty, which was more significant near the wall. Neither profile could be fitted well by the 1/7th law, but

Free stream velocity	USF	Uniform
$\overline{U}_{1\max}$ [m/s]	0.20	0.14
δ [m]	0.084	0.080
Re_x	$470,000$	$330,000$
Re_θ	$1,600$	$1,000$

Table 5.1: Properties of boundary layers at $x_1/h = 5.1$ with a uniformly sheared free stream and a uniform free stream.

both profiles were, at least partially, closer to a 1/6th law. In summary, these results show that the presence of USF in the free stream has no measurable effect on the mean velocity profile inside the TBL in this facility.

Profiles of the streamwise velocity standard deviation at $x_1/h = 5.1$ in the two flows are shown in Figure 5.28. Even in the absence of USF, the free stream contained a significant level of disturbances (nearly 2%), originating in the injection of the recirculating water in the settling tank of the water tunnel and only partially dampened by flow conditioning screens and other devices placed upstream of the test section. Such level of free stream disturbances is higher than the one in many previous studies of canonical TBL and allows us to separate to some degree the effect of shearing in the free stream from the effect of non-sheared free stream turbulence. The same figure also indicates that the turbulence in the near-wall part of the TBL ($x_2/\delta \lesssim 0.2$) was not affected visibly by the presence of USF, whereas, further away ($0.2 \lesssim x_2/\delta < 1$), the presence of USF increased measurably the turbulence level. This increase could be attributed to the overall higher turbulence level in the USF, by comparison to that in the uniform free stream, but could also be in part due to the penetration of coherent structures from the USF into the TBL.

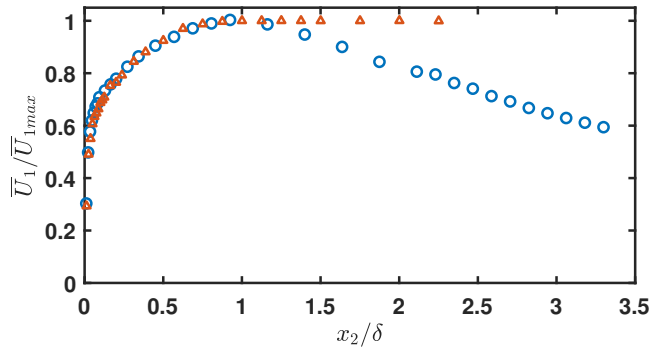

Figure 5.26: Profiles of the normalised mean streamwise velocity at $x_1/h = 5.1$ in and near TBL with a uniform free stream (△) and a uniformly sheared free stream (○).

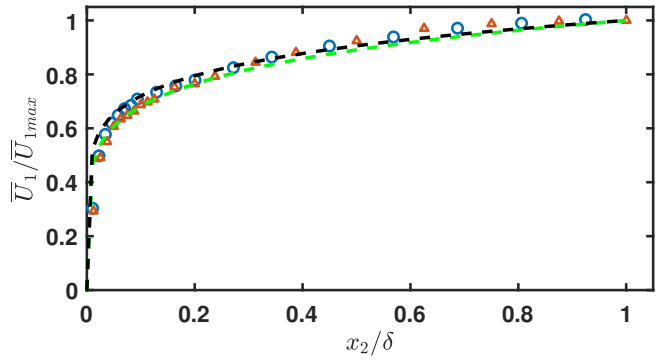

Figure 5.27: Profiles of the mean streamwise velocity at $x_1/h = 5.1$ inside TBL with a uniform free stream (△) and a uniformly sheared free stream (○); the thin black line marks the 1/7th law and the dashed green line marks the 1/6th law.

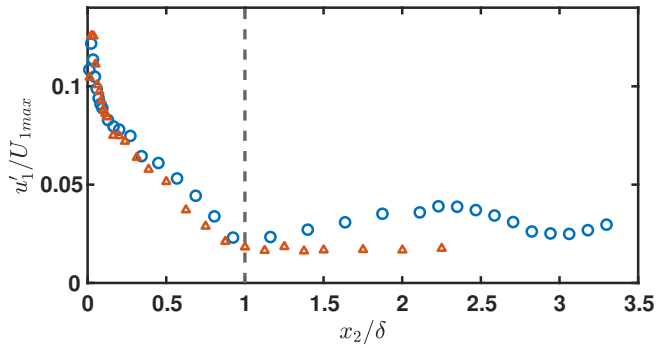

Figure 5.28: Profiles of the streamwise velocity standard deviation at $x_1/h = 5.1$ in and near TBL with a uniform free stream (△) and a uniformly sheared free stream (○).

5.7 Coherent structures

5.7.1 The vortex heads

Figure 5.29 shows representative instantaneous velocity maps obtained with the PIV system on the vertical centreplane of the test section at two different elevations and two streamwise stations. As mentioned in previous sections, it is well known that the dominant coherent structures in both the TBL and the USF are horseshoe vortices. The orientations of such vortices are random, but their axes are on the average inclined with respect to the flow direction and lie on a plane that includes the mean velocity and its gradient. Consequently, if a vertical cross-section of the flow, shown by the images in Figure 5.29, intersected the legs of the horseshoes, it would on the average do so nearly parallel to their axes, namely on a plane that has very little, if any, swirl. On the other hand, if the same vertical plane intersected the head of a horseshoe, it would do so nearly normal to the local vortex axis direction, which is a plane with a strong swirl. We may, therefore infer that the ellipses fitted on these images, at least the ones that contain strong swirl, are mostly cross-sections of vortex heads.

As these images are oriented such that the flow is from left to right and the wall is towards the top of the image, one would expect that the vortices produced by wall-generated shear would appear as counter-clockwise (CCW – ellipses with black

contours in Figure 5.29), whereas the ones that are produced by the USF would appear as clockwise (CW – ellipses with white contours). It is noted that the sense of rotation of vortex heads produced by each of the two mechanisms would be the same for upright and inverted horseshoes, which means that vertical images cannot distinguish upright from inverted horseshoes. The images also show flood maps of the velocity magnitude. As shown previously for both canonical TBL (de Silva et al., 2016) and undistorted USF (Vanderwel and Tavoularis, 2016), the flow velocity field does not change continuously across the test section, but consists of zones of nearly uniform velocity. The presented images illustrate that vortices tend to cluster at the boundary between such zones, in conformity with the literature.

Although the appearance of the images in Figure 5.29 changes in time, and some numbers of both CW and CCW vortices can be identified across the flow, one may confirm qualitatively that the majority of vortices well inside the TBL are CCW, those well inside the USF are CW, and those in the multi-structure region are mixed.

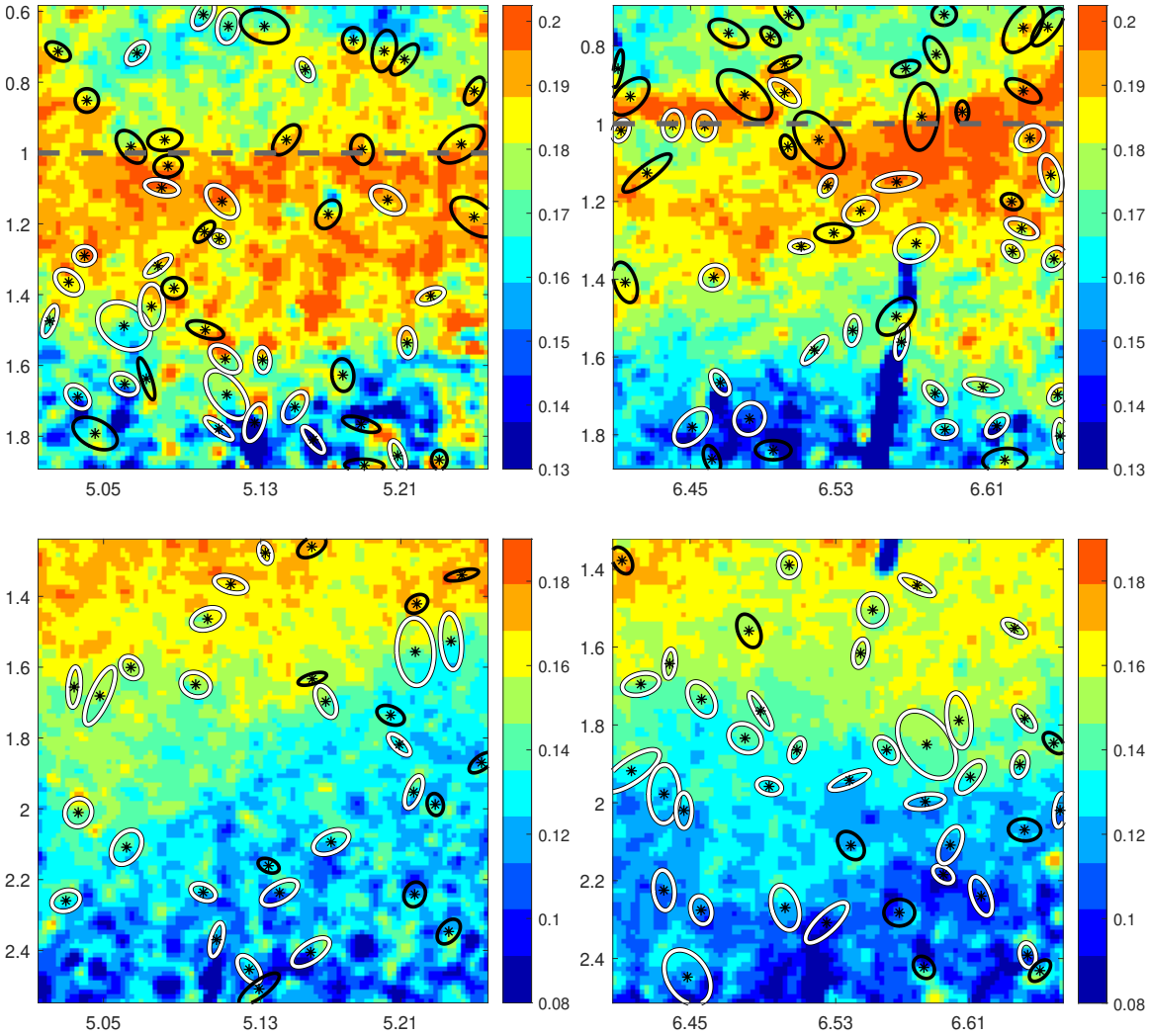

Figure 5.29: Representative instantaneous velocity maps on the vertical (x_1, x_2) centreplane of the test section at two different elevations (top and bottom rows, respectively, with increasing distance from the wall) and two streamwise locations ($x_1/h \approx 5.1$ in the left column and 6.5 in the right column); numbers on the ordinate denote the normalised distance from the wall (x_2/δ), numbers on the abscissa denote the normalised streamwise distance (x_1/h) and the legends (specific to each image) describe the velocity magnitude in m/s; the physical scales of both axes are the same; ellipses mark areas with relatively large swirl, which are interpreted to be cross sections of mostly vortex heads; white ellipse contours indicate clockwise rotation and black ones indicate counter-clockwise rotation.

5.7.2 The vortex legs

To assist with the interpretation of the horizontal velocity maps, Figure 5.30 shows an idealised sketch of two types of upright horseshoe vortices: one that would likely be generated by the shear near the wall and another that would likely be generated by the free shear in the USF. The heads of both horseshoes are downstream of their legs and toward the direction of increasing local mean velocity. This makes the heads of the TBL horseshoes pointing away from the wall, in contrast to the heads of the USF horseshoes that point toward the wall. Although a three-dimensional map of the velocity field would clearly reveal the type of horseshoe in question, the signatures of the two types on a horizontal plane are hard to distinguish from each other: both induce a velocity field that tends to bring lower-speed fluid between their legs on the respective horizontal plane; and, in both cases, the cross-section of the clockwise-rotating leg is at a spanwise location with a larger x_3 than that of the counter-clockwise leg. Inverted vortices would have the same average inclination as the upright ones, but their head would be on the opposite end of the legs. It would be equally difficult to distinguish between TBL and USF inverted horseshoes based on their horizontal signatures. On the other hand, it is possible to distinguish them from upright horseshoes, because the former transport higher-speed fluid between their legs and, moreover, because the cross-section of the CCW leg would be at a spanwise location with a larger x_3 than that of the CW leg. In summary, the location and appearance of presumed, paired, horizontal cross-sections of horseshoe vortex legs may identify upright and inverted horseshoes, but not distinguish whether these horseshoes originate in the TBL or the USF, a trait that would have been desirable for the multi-structure region. Even so, horizontal velocity maps provide other useful information and so will be examined in the following.

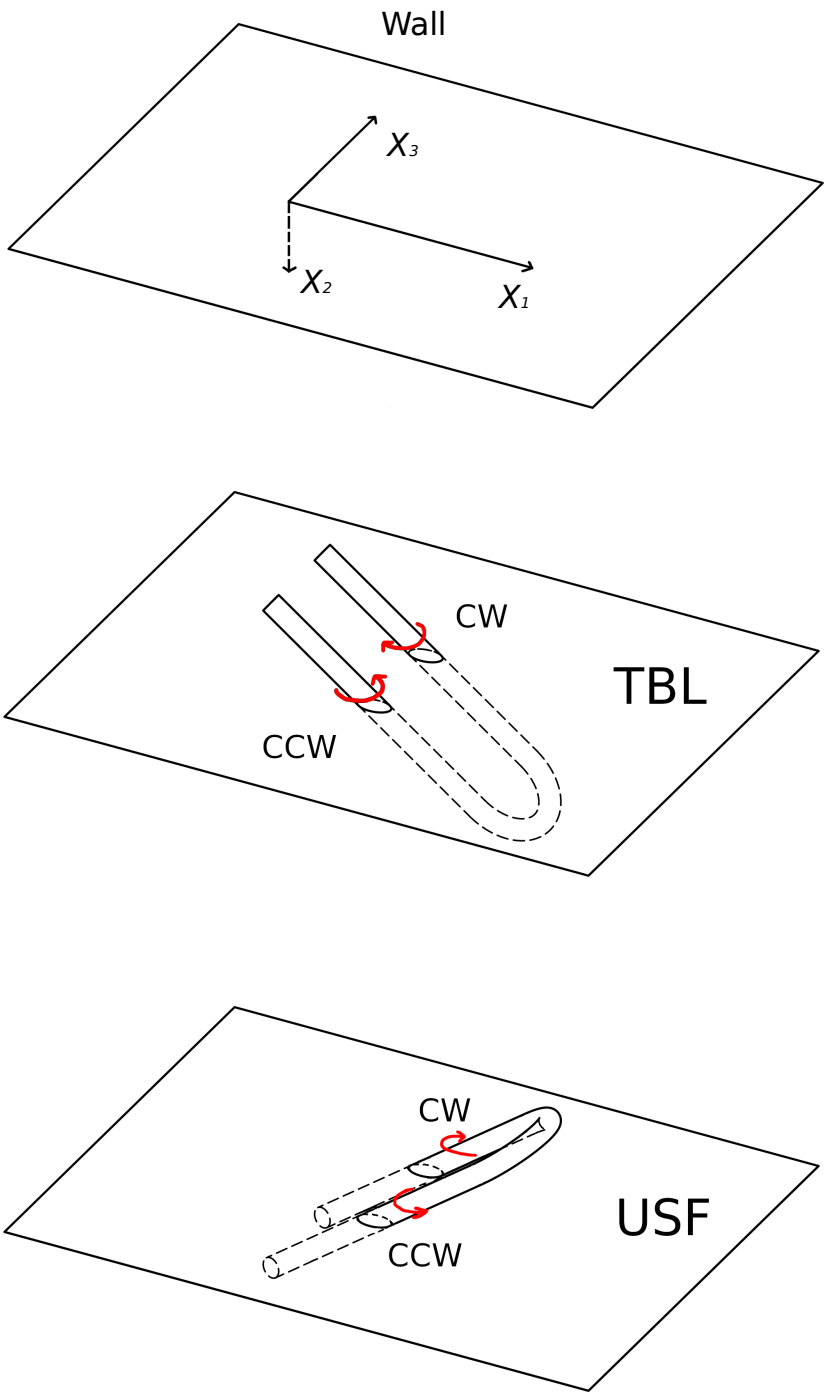

Figure 5.30: Sketch of idealised upright horseshoe vortices generated by wall shear in the TBL and by free shear in the USF, also marking the clockwise (CW) and counterclockwise (CCW) legs of each vortex.

Figure 5.31 shows representative instantaneous velocity maps obtained with the PIV system on horizontal planes of the test section at four different elevations and two streamwise stations. Unfortunately, the recorded set does not include images at or very close to the TBL edge, which is central to the multi-structure region, but includes sets of images on either side of the edge and within the multi-structure region. Each image contains a multitude of ellipses with black (CCW) and white (CW) contours, many of which can be matched to form a pair, deemed to represent cross-sections of the legs of a horseshoe vortex. To illustrate this point, examples of such pairs have been marked in Figure 5.31c by lines connecting the axes of two neighbouring ellipses. These examples demonstrate that the two legs of each horseshoe are typically on either side of a high-speed or a low-speed zone. Five neighbouring upright horseshoes, with legs connected by red lines, are seen to straddle a low-speed zone and five inverted horseshoes, with legs connected by purple lines, are seen to straddle a high-speed zone. This example indicates that horseshoes often appear in packets, in conformity with the literature (Adrian, 2007; Vanderwel and Tavoularis, 2011). This image is within the multi-structure region, but unfortunately, it is not possible to assert whether either of these packets originates in the TBL or the USF.

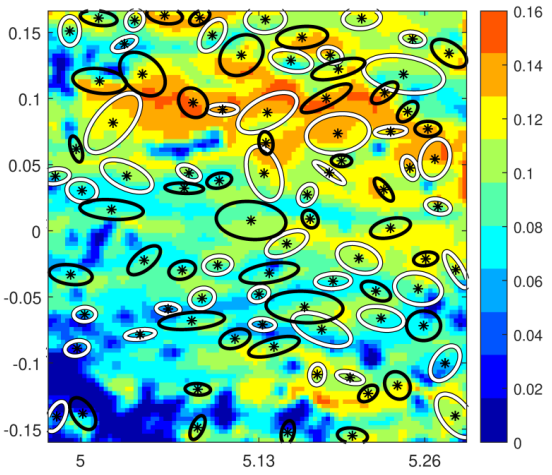

(a) $x_2/\delta = 0.14$

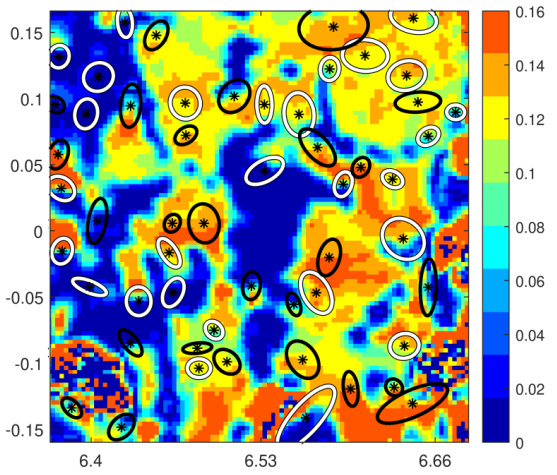

(b) $x_2/\delta = 0.13$

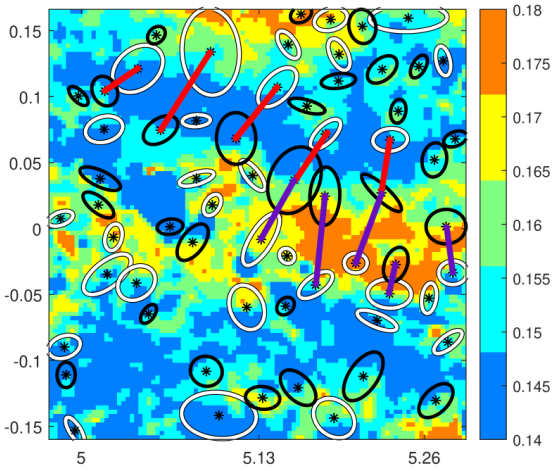

(c) $x_2/\delta = 0.67$

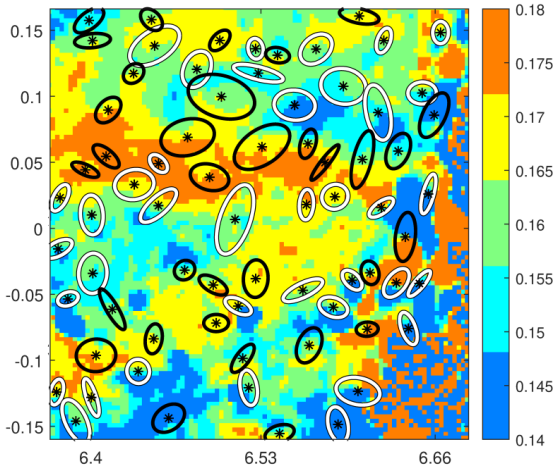

(d) $x_2/\delta = 0.61$

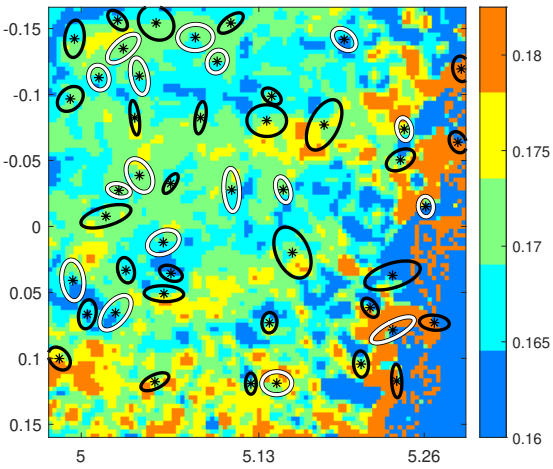

(e) $x_2/\delta = 1.00$

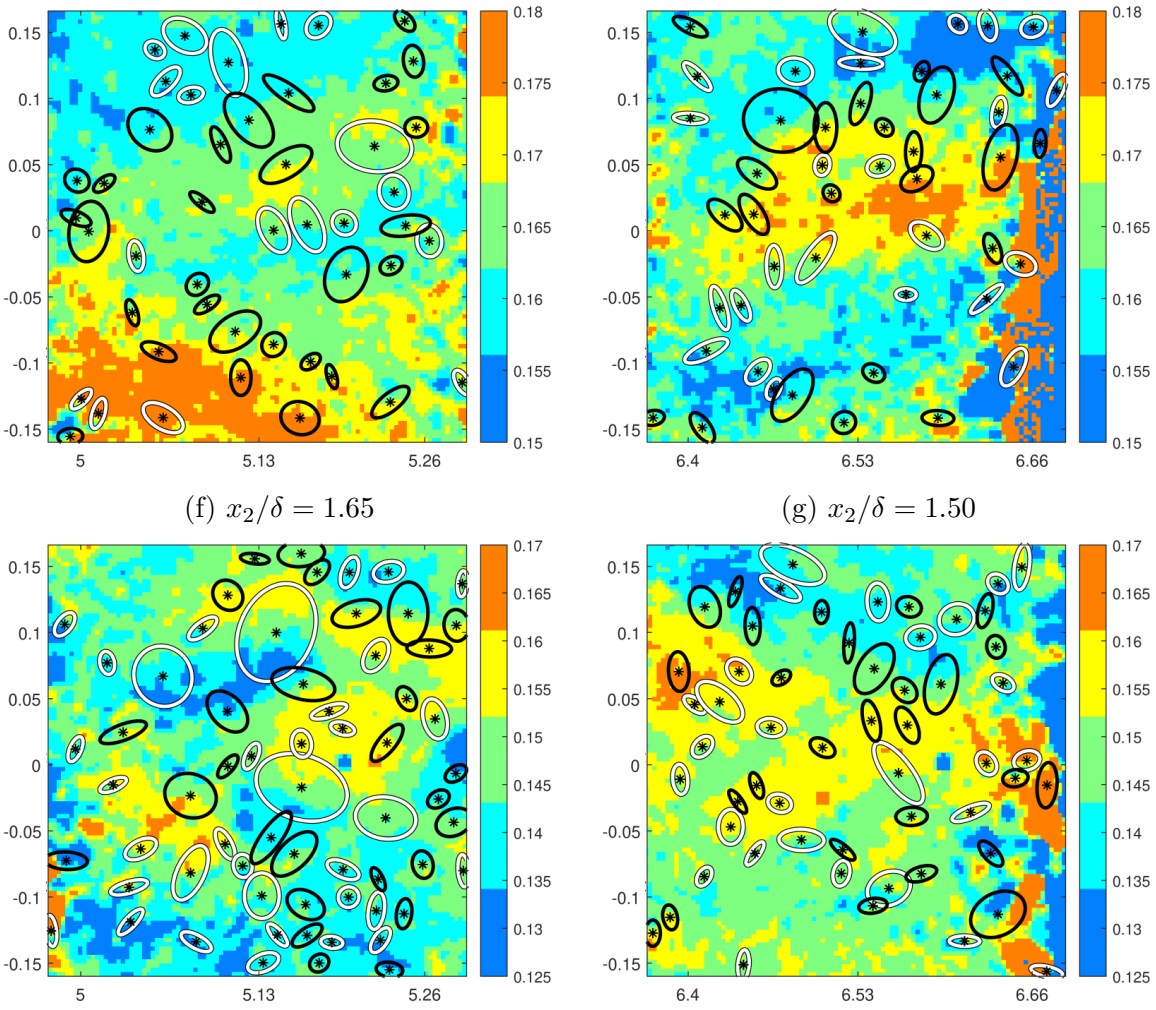

(f) $x_2/\delta = 1.65$ (g) $x_2/\delta = 1.50$

(h) $x_2/\delta = 2.18$ (i) $x_2/\delta = 1.98$

Figure 5.31: Representative instantaneous velocity maps on horizontal (x_1, x_3) planes at four different elevations (shown from the top to the bottom row with increasing distance from the wall) and two streamwise locations ($x_1/h \approx 5.1$ in the left column and 6.5 in the right column); numbers on the ordinate denote the normalised streamwise distance (x_1/h), numbers on the abscissa denote the normalised spanwise distance from the centreplane (x_3/h) and the legends (specific to each image) describe the velocity magnitude in m/s; the physical scales of both axes are the same; ellipses mark areas with relatively large swirl, which are interpreted to be cross sections of mostly vortex legs; white ellipse contours indicate clockwise rotation and black ones indicate counter-clockwise rotation; red or black lines connect the axes of selected vortex pairs, deemed to be the legs of, respectively, upright or inverted horseshoes.

The properties of the ellipses in sub-populations of the 350 horizontal velocity maps that were recorded at each location were determined by visual inspection in

an effort to determine how coherent structures changed across the flow. It is recognised that the uncertainty of the corresponding estimates is considerable and so the following observations are mostly of qualitative significance.

Table 5.2 shows the densities of all vortices, the densities of CW and CCW vortices and the densities of upright and inverted horseshoes on planes at four different distances from the wall and two streamwise stations. The sum of upright and inverted horseshoes is significantly lower than half the total number of vortices, as a considerable number of individual vortices cannot be reliably matched with another. It is evident, both from the values shown in the table and the images shown in Figure 5.31, that there are more vortices of all types in the TBL than in the multi-structure region and the USF. In all regions, however, the densities of CW and CCW vortices were nearly the same and the densities of upright and inverted horseshoes were also roughly the same. The latter observation conforms with the literature as far as USF is concerned (Vanderwel and Tavoularis, 2011), but seems to be a novel one for TBL.

$x_1/h = 5.1$						$x_1/h = 6.5$					
x_2/δ	Total	CW	CCW	Up.	Inv.	x_2/δ	Total	CW	CCW	Up.	Inv.
0.14	56	27	29	10	11	0.13	69	34	35	6	9
0.67	48	23	25	8	6	0.61	60	30	30	9	14
1.00	30	16	14	6	5						
1.65	33	18	15	6	7	1.50	29	14	15	6	5
2.17	36	18	18	6	4	1.98	42	21	21	7	8

Table 5.2: Number of vortices in a horizontal area equal to δ^2. Columns correspond to the total number of vortices, clockwise vortices, counter-clockwise vortices, upright horseshoes and inverted horseshoes.

Another piece of information that was extracted from the images was the average inclination of the horseshoes with respect to the horizontal plane. This property was determined from the aspect ratio of the ellipses, under the assumption that each ellipse is a cross-section of a cylindrical vortex. Our analysis indicated that this inclination spanned a wide range, but, on the average, was roughly 55° at all four elevations. This value is somewhat larger than values reported in the TBL and USF literature.

Figure 5.32 presents the average circulation magnitude for all vortices *vs.* the normalised distance from the wall. Despite the considerable scatter, one may assert

that the vortices, viewed as a whole, are stronger in the undisturbed part of the TBL, they are weaker in the USF, and they have an intermediate strength in the multi-structure region.

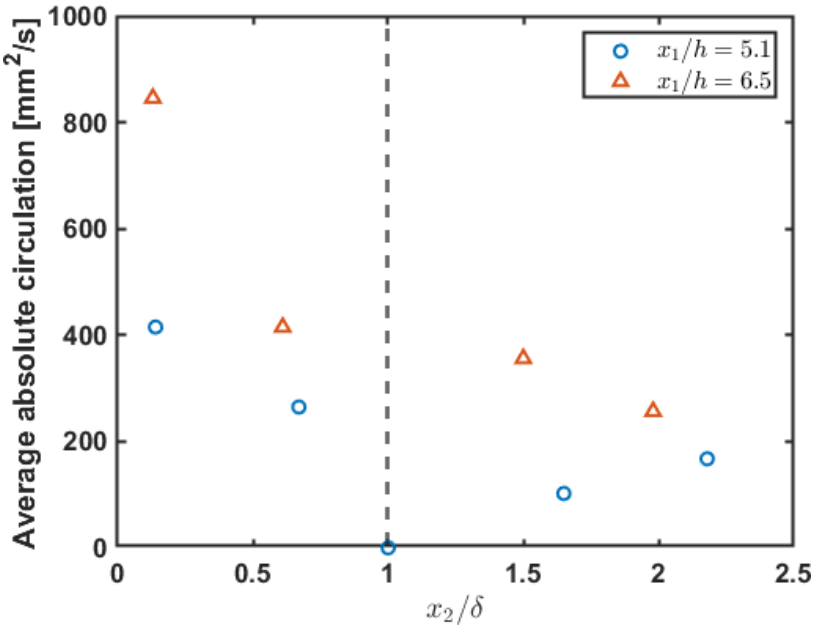

Figure 5.32: Average circulation magnitude of all vortices on a horizontal plane *vs.* normalised distance from the wall.

5.7.3 Coherent structures *vs.* length scales

The present data provide an opportunity to test past postulations about the relationship between geometrical properties of coherent structures and turbulence length scales. Such tests will be performed in the undisturbed TBL region, the undisturbed USF, as well as the multi-structure region between the two. For these tests, we inspected visually a number of horizontal images at each location and identified those horseshoe vortices that fitted the general pattern of a pair of counter-rotating vortices on either side of a high-speed or low-speed zone. We then determined the following properties:

- the average distance W between the midpoint of the line segment connecting the axes of the two vortices in each pair and the corresponding midpoint of the

closest vortex pair that was not straddling the same low-speed or high-speed streak;

- the average length w of the line segment connecting the axes of the two vortices in each matched pair; and

- the average diameter d of all vortices in pairs, considered to be the shorter of the two dimensions of each ellipse.

Tennekes (1968) has connected w to the Taylor microscale λ and d to the Kolmogorov microscale η. Speculation in the general turbulence community has further associated W with the integral length scale L. To test these hypotheses, we estimated roughly the average ratios W/L, w/λ and d/η at the selected locations and listed their values in Table 5.3. It was found that $W/L \approx 0.89 \pm 0.10$ throughout the height of the test section. Moreover, $w/\lambda \approx 1.8 \pm 0.3$ for the majority of the examined distances from the wall, but much larger (≈ 6) at $x_2/\delta = 1$. The ratio d/η was found to be ≈ 19 at the location nearest to the upper wall but $\approx 12 \pm 2$ at the other four distances from the wall. In summary, one may conclude that the spacing between neighbouring horseshoe vortices is fairly representative of the integral length scale. Although the distance between horseshoe leg cross-sections on the image plane is nearly twice the Taylor microscale, most horseshoes would have a random spanwise inclination with respect to the horizontal plane and so the shortest distance between their legs would be smaller than w; this essentially validates Tennekes' postulate. Finally, the vortex diameter appears to be an order of magnitude larger than the Kolmogorov microscale. Once more, it is noted that, due to the random spanwise inclination of the vortices, the actual vortex diameter would be somewhat smaller than the reported value. Moreover, the diameter produced by the present ellipse-fitting algorithm does not necessarily match the concept of a vortex tube diameter in Tennekes' article. Even with these considerations, our estimate of vortex diameter is sufficiently larger than η as not to serve as a fair estimate of it.

$x_1/h = 5.1$				$x_1/h = 6.5$			
x_2/δ	W/L	w/λ	d/η	x_2/δ	W/L	w/λ	d/η
0.14	0.89 (27)	2.2 (57)	20 (66)	0.13	0.85 (38)	2.0 (57)	18 (66)
0.67	0.85 (20)	1.7 (57)	13 (69)	0.61	0.70 (25)	1.7 (57)	15 (66)
1.00	0.81 (28)	5.9 (57)	11 (66)				
1.65	0.88 (24)	2.0 (57)	11 (66)	1.50	0.97 (26)	1.4 (57)	8 (66)
2.17	1.01 (27)	1.8 (57)	13 (65)	1.98	0.78 (27)	1.2 (57)	10 (66)

Table 5.3: Average ratios of specific geometrical properties of the horseshoe vortex field and corresponding length scales at selected locations across the flow; the number of cases considered for each average is shown in parentheses.

Chapter 6

Conclusions and recommendations for future work

6.1 Conclusions

The main findings of this work can be summarised as follows.

- For the first time, a turbulent boundary layer was generated in the laboratory with a highly turbulent free stream that consisted of a uniformly sheared flow with a mean shear direction that was opposite to the direction of wall-generated shear.

- Although the mean velocity profile in the inner TBL did not match well the canonical 1/7th power law, the growth rates of the physical and momentum boundary layer thicknesses were close to those in canonical TBL. The maximum velocity at the boundary layer edge, considered to be the free stream velocity was nearly constant and so the boundary layer Reynolds numbers also grew at nearly canonical rates.

- The turbulence properties in the near-wall half of the TBL ($0 \leq x_2/\delta \lesssim 0.5$) were comparable to canonical ones and those sufficiently away from the wall ($2 \lesssim x_2/\delta$) were comparable to those in canonical USF. Such properties were, however, measurably non-canonical in the intermediate region ($0.5 \lesssim x_2/\delta \lesssim 2$), which can be characterised as a multi-structure region. The mean shear in the multi-structure region was lower than outside it and the turbulence anisotropy was lower in the multi-structure region as well. The turbulent shear stress variation across the flow was consistent with gradient transport.

- The integral length scale in the outer TBL was comparable to the one in the USF and so its value did not change measurably in the multi-structure region. The

Taylor and Kolmogorov microscales exhibited nearly canonical trends outside the multi-structure region but had distinct patterns within this region.

- A prominent feature of the multi-structure region is that the dissipation parameter had significantly larger values than those outside it, which were canonical. The turbulence Reynolds number in the multi-structure region was lower than canonical and one may roughly describe the variation of C_ϵ across the multi-structure region as inversely proportional to the local Re_λ.

- Instantaneous velocity maps on planes that contained the streamwise direction and the direction normal to the wall revealed the presence of vortices, which were interpreted as mostly cross-sections of heads of horseshoe-shaped coherent structures. It was hypothesised that counter-clockwise vortices were produced by wall-generated mean shear, whereas clockwise vortices were produced by free shear in the USF. Both vortex types were observed across the flow, but the balance between the two types was much more even in the multi-structure region than outside it.

- Instantaneous velocity maps on horizontal planes at different distances from the wall revealed the presence of many vortices, several of which could be matched as counter-rotating pairs that were interpreted as cross-sections of the legs of horseshoe structures. Vortex packets were observed, straddling low-speed or high-speed streaks. Both upright and inverted horseshoe vortices were identified in all of the horizontal planes but the images could not discriminate between vortices produced by the two shear mechanisms. The density of horseshoes was greatest within the undistorted TBL region.

- The distance between vortices that do not belong to the same packet was found to be comparable to the integral length scale. The distance between the legs of horseshoes was comparable to, although somewhat larger than, the Taylor microscale. The diameter of vortices was an order of magnitude larger than the Kolmogorov microscale.

6.2 Recommendations for future research

The following recommendations are made for extending the work described in this thesis.

- A theoretical justification for the inverse proportionality of C_ϵ and Re_λ, which was presently observed in the TBL/USF multi-structure region, as well as by previous investigators in other non-canonical flows, would be a key discovery. This would pave the way towards understanding the scaling of turbulent kinetic dissipation rate in complex flows and the development of more powerful turbulence models than presently available.

- A documentation of a TBL extending to a uniform, low-turbulence free stream in the same facility would clarify the non-canonical behaviour of the inner region of the present TBL.

- As the non-canonical behaviour in the multi-structure region at $x_1/h = 6.5$ seemed to be milder than that at $x_1/h = 5.1$, it would be of interest to extend the measurements to longer streamwise distances from the origin.

- Additional horizontal velocity maps at and close to the TBL edge would be useful to further illuminate the coherent structure pattern in the multi-structure region.

- Stereoscopic PIV measurements would assist in understanding the three-dimensional character of the coherent structures and discriminate between wall-shear- and free-shear-generated horseshoe vortices.

References

Adrian, R. J. Hairpin vortex organization in wall turbulence. *Phys. Fluids*, 19(4): 041301, 2007. doi: 10.1063/1.2717527.

Adrian, R. J., Meinhart, C. D., and Tomkins, C. D. Vortex organization in the outer region of the turbulent boundary layer. *J. Fluid Mech.*, 422:1–54, 2000. doi: 10.1017/s0022112000001580.

Burattini, P., Lavoie, P., and Antonia, R. A. On the normalized turbulent energy dissipation rate. *Phys. Fluids*, 17(9):098103, 2005. doi: 10.1063/1.2055529.

Charnay, G., Comte-Bellot, G., and Mathieu, J. Development of a turbulent boundary layer on a flat plate. In *Turbulent Shear Flows*, pp. 27.1–27.10. Technical Editing and Reproduction Ltd, 1971.

Dantec Dynamics. Fluid Mechanics. URL `https://www.dantecdynamics.com/solutions-applications/solutions/fluid-mechanics/`.

de Silva, C. M., Hutchins, N., and Marusic, I. Uniform momentum zones in turbulent boundary layers. *J. Fluid Mech.*, 786:309–331, 2016. doi: 10.1017/jfm.2015.672.

Djenidi, L., Lefeuvre, N., Kamruzzaman, M., and Antonia, R. A. On the normalized dissipation parameter in decaying turbulence. *J. Fluid Mech.*, 817:61–79, 2017. doi: 10.1017/jfm.2017.110.

Dong, S., Lozano-Durán, A., Sekimoto, A., and Jiménez, J. Coherent structures in statistically stationary homogeneous shear turbulence. *J. Fluid Mech.*, 816:167–208, 2017. doi: 10.1017/jfm.2017.78.

Evans, R. L. Free-stream turbulence effects on the turbulent boundary layer. *Aeronautical Research Council Current Papers No. 1282*, 1974.

Head, M. R. and Bandyopadhyay, P. New aspects of turbulent boundary-layer structure. *J. Fluid Mech.*, 107(1):297–338, 1981. doi: 10.1017/s0022112081001791.

Hoffmann, J. A., Kassir, S. M., and Larwood, S. M. The influence of free-stream turbulence on turbulent boundary layers with mild adverse pressure gradients. Technical Report 177520, NASA, Ames Research Center, 1989.

Kida, S. and Tanaka, M. Reynolds stress and vortical structure in a uniformly sheared turbulence. *J. Phys. Soc. Jpn.*, 61(12):4400–4417, 1992. doi: 10.1143/jpsj.61.4400.

Kislich-Lemyre, B. C. *The large-scale structure of uniformly sheared turbulence and its distortion by a solid wall at rest or in motion*. PhD thesis, University of Ottawa, 2003.

Liangwei, Fang and Hoffmann, J.A. Effects of anisotropic free-stream turbulence on turbulent boundary layer behavior. In Yuan, Shen, editor, *Frontiers of Fluid Mechanics*, pp. 56 – 61. Pergamon, 1988. ISBN 978-0-08-036232-8. doi: https://doi.org/10.1016/B978-0-08-036232-8.50015-3. URL `http://www.sciencedirect.com/science/article/pii/B9780080362328500153`.

Mazellier, N. and Vassilicos, J. C. The turbulence dissipation constant is not universal because of its universal dependence on large-scale flow topology. *Phys. Fluids*, 20 (1):015101, 2008. doi: 10.1063/1.2832778.

Meier, H. U. and Kreplin, H.-P. Influence of freestream turbulence on boundary-layer development. *AIAA Journal*, 18(1):11–15, 1980. doi: 10.2514/3.50724.

Nedić, J. and Tavoularis, S. Energy dissipation scaling in uniformly sheared turbulence. *Phys. Rev. E*, 93(3), 2016. doi: 10.1103/physreve.93.033115.

Nedić, J. and Tavoularis, S. A case study of multi-structure turbulence: Uniformly sheared flow distorted by a grid. *Int. J. Heat Fluid Flow*, 72:233–242, 2018. doi: 10.1016/j.ijheatfluidflow.2018.06.010.

Nedić, J., Tavoularis, S., and Marusic, I. Dissipation scaling in constant-pressure turbulent boundary layers. *Phys. Rev. Fluids*, 2(3), 2017. doi: 10.1103/physrevfluids.2.032601.

Pearson, B. R., Krogstad, P.-Ã., and Water, W. Van De. Measurements of the turbulent energy dissipation rate. *Phys. Fluids*, 14(3):1288–1290, 2002. doi: 10.1063/1.1445422.

Robinson, S. K. Coherent motions in the turbulent boundary layer. *Annu. Rev. Fluid Mech.*, 23(1):601–639, 1991. doi: 10.1146/annurev.fluid.23.1.601.

Rogers, M. M. and Moin, P. The structure of the vorticity field in homogeneous turbulent flows. *J. Fluid Mech.*, 176:33–66, 1987. doi: 10.1017/s0022112087000569.

Sakai, Y., Hiruta, K., Nagata, K., Suzuki, H., and Terashima, O. Effects of the cylinder wake in a freestream on statistical properties of a turbulent boundary layer. *Transactions of the JSME (in Japanese)*, 79(799):64–76, 2013. doi: 10.1299/transjsme.14-00582.

Tennekes, H. Simple model for the small-scale structure of turbulence. *Phys. Fluids*, 11(3):669–671, 1968.

Theodorsen, T. Mechanisms of turbulence. *Proceedings of the Second Midwestern Conference on Fluid Mechanics*, 1952. URL https://ci.nii.ac.jp/naid/10016445071/en/.

Vanderwel, C. and Tavoularis, S. Coherent structures in uniformly sheared turbulent flow. *J. Fluid Mech.*, 689:434–464, 2011. doi: 10.1017/jfm.2011.423.

Vanderwel, C. and Tavoularis, S. Scalar dispersion by coherent structures in uniformly sheared flow generated in a water tunnel. *J. Turbul.*, 17(7):633–650, 2016. doi: 10.1080/14685248.2016.1155713. URL https://doi.org/10.1080/14685248.2016.1155713.

Vanderwel, C. M. Coherent structures in uniformly sheared turbulence. Master's thesis, University of Ottawa, 2009.

Vassilicos, J. C. Dissipation in turbulent flows. *Annu. Rev. Fluid Mech.*, 47(1):95–114, 2015. doi: 10.1146/annurev-fluid-010814-014637.

Wu, X and Moin, Pa. Direct numerical simulation of turbulence in a nominally zero-pressure-gradient flat-plate boundary layer. *J. Fluid Mech.*, 630:5–41, 2009. doi: 10.1017/s0022112009006624.